Novel Economic Analysis to Design the Energy Storage Control System of a Remote Islanded Microgrid

Giovanna Oriti, *Senior Member, IEEE*, Alexander L. Julian, *Senior Member, IEEE*, Norma Anglani, *Member, IEEE*, and Gabriel D. Hernandez

***Abstract*—This paper presents a novel power flow control strategy, combined with an economic analysis, for an energy management system (EMS) involving a hybrid energy storage. The EMS operates a remote microgrid and directs the power flow to either batteries or supercapacitors to increase the life of the batteries. This paper demonstrates how the use of supercapacitors increases the lifetime of the batteries and ultimately how it affects the economics of the system. The proposed EMS controller also compensates for the 120-Hz ripple on the dc bus. Modeling, simulations, and experimental verification are presented together with the procedure to perform the assessment of the battery lifetime, according to the tuning parameters of the controller.**

***Index Terms*—Battery lifetime, energy management, hybrid energy storage, power converters, supercapacitors (SCs).**

I. Introduction

MICROGRID technology has been developed and closely investigated as one of the solutions to increase energy security. Solid-state power converters are instrumental to microgrid operations [1]. Power-electronics-based energy management systems (EMS) have been recently explored (see [2]–[8]) to control loads and distributed energy resources (DERs), to detect grid failure, and to enable the microgrid islanding mode of operation. Although an EMS is sometimes used to define the software or controller that manages the energy in a power system or microgrid, in this paper, it is used to define a system, which includes one or more power converters that interface to a microgrid and different DERs. In addition to the hardware, the EMS includes several layers of control to manage currents and voltages, as well as loads and sources. An EMS has been recently proposed to optimize operations in remote military microgrids, where continuous service to critical power loads is essential [5], [8]. In this paper, we focus on the EMS ability to control the power flow when a hybrid energy storage system (HESS) is added to the architecture because the real load profile, showing sudden peaks, is considered [9]. The goal of the proposed HESS is to divert the 120-Hz ripple and the peak current ripple away from the batteries by adding supercapacitors (SCs) controlled by a buck–boost converter, thus increasing the lifetime expectation of the batteries available in the microgrid. A novel study to tune the controllers parameters is carried out for a remote military microgrid model. Recent publications [10]–[19] have addressed hybrid storage systems with batteries and SCs in different configurations. Some HESS configurations have used different power converter topologies and controllers [10], [11], [15], or they do not show a thorough analysis of the control system [6]. In [20], the focus is exclusively the energy management of a light rail vehicle; therefore, the power electronics controller is not addressed.

Other HESS do not control the 120-Hz ripple on the dc bus either because they are applied to three-phase systems [16] or because they service loads that are not single-phase ac [12], [21]. Papers [17] and [18] present HESS controllers that are very similar to the one proposed in this paper, but they do not include the battery lifetime analysis nor the application to the economics of a microgrid as they are presented in this paper. In [19], although a similar HESS controller was used, the power management strategy used has a different scope than the one proposed in this paper; losses and state of charge (SoC) of the SCs are weighted to be optimized, but the authors do not quantify how this procedure affects the expectation of battery lifetime extension. In [22], an interesting application of optimal power flow problem with the HESS is considered, but time steps are bigger (30 s versus our 0.1 s), and no consideration on investments is included: the economic is based on the cost of the saved energy, thus neglecting the role of sizing, which we show is also a key issue when dealing with the HESS. Here, we evaluate how the different controller strategies, implemented with a proper number of SCs, can increase the battery lifetime.

Manuscript received November 27, 2017; revised March 4, 2018; accepted June 7, 2018. Paper 2017-SECSC-1138.R1, presented at the 2017 IEEE Energy Conversion Congress and Exposition, Cincinnati, OH, USA, Oct. 1–5, and approved for publication in the IEEE Transactions on Industry Applications by the Renewable and Sustainable Energy Conversion Systems Committee of the IEEE Industry Applications Society. This work was supported in part by the U.S. Office of Naval Research as part of the Energy Systems Technology Evaluation Program. *(Corresponding author: Norma Anglani.)*

G. Oriti is with the Naval Postgraduate School, Monterey, CA 93943 USA (e-mail: goriti@nps.edu).

A. L. Julian was with the Naval Postgraduate School, Monterey, CA 93943, USA. He is now a consultant in Seaside, CA, USA (e-mail: alexander.julian@ieee.org).

N. Anglani is with the University of Pavia, 27100 Pavia, Italy (e-mail: nanglani@unipv.it).

G. D. Hernandez is an Engineering Duty Officer with Portsmouth Naval Shipyard, Kittery, ME 03904 USA (e-mail: gabe.hernandez@live.com).

Color versions of one or more of the figures in this paper are available online at http://ieeexplore.ieee.org.

Digital Object Identifier 10.1109/TIA.2018.2853041

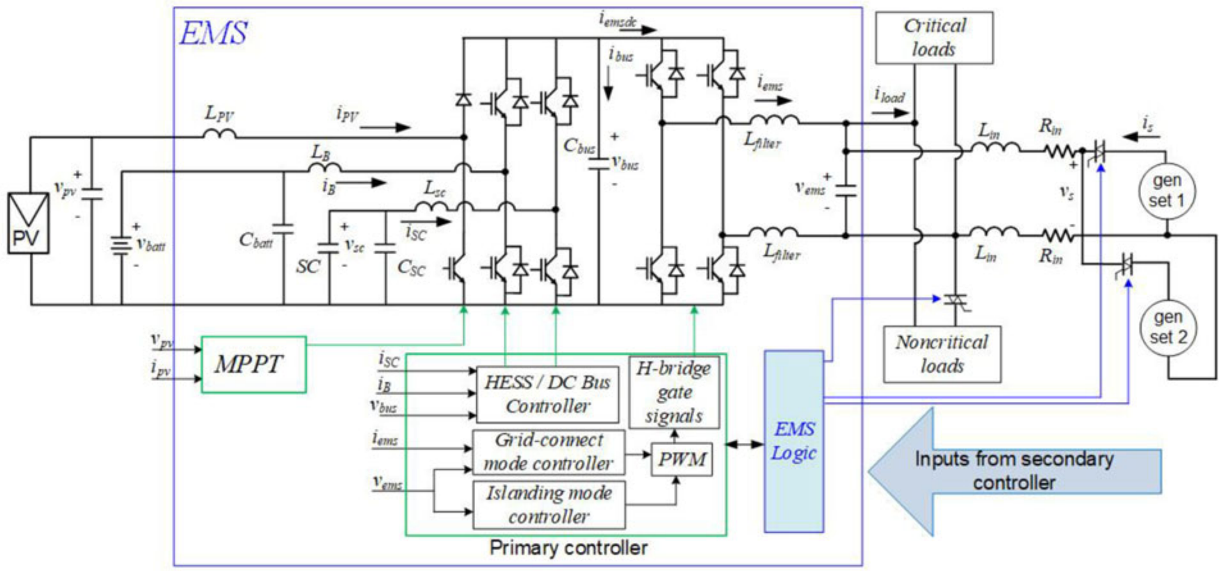

Fig. 1. EMS architecture and its connection to a remote military microgrid with two diesel generators, hybrid energy storage, and PV panels.

To the knowledge of these authors, the proposed combination of a buck–boost converter, a control architecture, and a tight link with the battery lifetime presented in this paper has not been previously presented. Furthermore, the application to a remote microgrid introduces peculiarities in the economics of the considered case study. In this paper, the EMS architecture is presented in Section II. The proposed HESS controller is described in Section III. In Section IV, the procedure, involving the battery lifetime and its link with a specific controller parameter, is presented for a typical power profile of a remote military microgrid. Experimental measurements and conclusions are reported in Sections V and VI, respectively.

II. EMS Functionality and Microgrid Setup

A schematic of the EMS' architecture is provided in Fig. 1 together with the remote military microgrid power system. Also shown in Fig. 1 are critical and noncritical loads and two diesel generator sets (gensets). Critical loads are those loads, including computers, radars, and some air conditioning systems, which are critical to the military operations success and must be powered at all times. Thus, they are hard wired to the ac power bus, while noncritical loads are connected to the ac bus through a solid-state switch controlled by the EMS to enable shedding when necessary. In this setup, the noncritical loads are grouped together for ease of laboratory demonstration; however, an EMS can control multiple noncritical load switches.

The EMS consists of five inverter legs, a field-programmable gate array (FPGA)-based control system, photovoltaic (PV) panels, battery pack, and SCs. Lead–acid batteries are used for the work presented in this paper; however, any other type of battery could be used, and this is true as far as the methodology concerns. However, lead–acid batteries are presently the technology of choice in remote military camps because they fail without catching fire, unlike Li-ion batteries. The FPGA-based controller includes the dc-bus voltage controller, the ac-bus voltage control during islanding operations, and the EMS ac current in the grid-connected mode. This paper focuses on a new dc-bus voltage controller, while the ac current and voltage control systems are the same as presented in [7]. The FPGA also houses the controls for the HESS and the energy management logic such as load scheduling and grid connect/disconnect. Two legs of the power module are employed as a single-phase bidirectional H-bridge converter, which can be controlled as a current source to inject power from the battery pack to the microgrid or as a voltage source when the gensets are OFF. The third leg of the power module is operated as a bidirectional buck–boost converter to either charge the battery bank or draw energy from it. The fourth leg of the power module is operated as a bidirectional buck–boost converter to either charge the SCs or draw energy from them. Batteries and SCs form the HESS, which is controlled by the EMS. A fifth inverter leg is used as a boost converter that is the interface to the PV panels.

III. HESS Control System

In this section, the HESS control system architecture is presented, and its functionality is demonstrated with analysis in the frequency-domain as well as time-domain simulations.

A. Controller Architecture and Functionality

The dc-bus voltage is held constant by the HESS controller shown in Fig. 2. In addition to regulating the dc bus, the goal of this controller is to distribute the load current between the battery and the SCs. Specifically, the load current is the current that the EMS injects into the ac bus to supplement the power provided by the generators. The peak current demanded by the loads is provided by the SCs instead of the battery to reduce the ac current stress on the battery. The low-pass filter commands the battery current to be absent of abrupt changes. The bandpass filter (BPF) is added to extract the 120-Hz signal, which has a

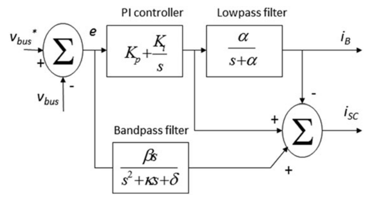

Fig. 2. HESS control system.

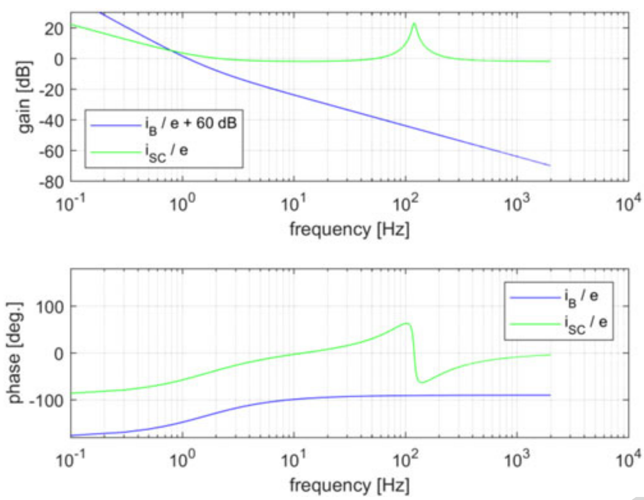

Fig. 3. Bode plots of battery current and SC current transfer functions.

frequency equal to twice the 60-Hz output frequency. The goal of the BPF is to reduce the second harmonic voltage ripple on the dc bus and ac current in the battery. The BPF is analyzed in the next section.

From the control diagram in Fig. 2, the transfer function of the battery current over the dc voltage error can be derived as

$$\frac{i_B}{e} = \frac{\alpha(sK_p + K_i)}{s(s+\alpha)}. \quad (1)$$

The dc voltage error leads to an SC current that is

$$\frac{i_{SC}}{e} = \frac{(sK_p + K_i)}{s} - \frac{\alpha(sK_p + K_i)}{s(s+\alpha)} + \frac{\beta s}{s^2 + \kappa s + \delta}. \quad (2)$$

The Bode plots of the transfer functions (1) and (2) are shown in Fig. 3. The battery current i_B contains only low-frequency components, while the SCs provide the current for any ac disturbances in the dc bus, especially at 120 Hz. In fact, the top plot in Fig. 3 shows that the gain of the transfer function (2) is high at 120 Hz. The parameters used for this analysis are shown in Table I.

B. Contribution and Analysis of the BPF

It is well known that a 120-Hz component is drawn from the dc bus by a single-phase inverter delivering 60-Hz ac power, so that pulsating power flows from the dc bus in addition to dc power. The role of the BPF in Fig. 3 is to ensure that the 120-Hz current is drawn from the SCs, not the batteries. The following analysis clarifies the contribution of the BPF.

The equivalent circuit in Fig. 4 represents the currents that are flowing to/from the EMS dc bus, which are the SC current

TABLE I
PARAMETERS OF THE CONTROLLER

Description	Symbol	Value
DC bus capacitor	C_{bus}	100 μF
Proportional gain	K_p	0.8
Integral gain	K_i	8
BPF coefficient	β	754
BPF coefficient	κ	57
BPF coefficient	δ	568,000
Low-pass filter coefficient	α	0.005 rad/s

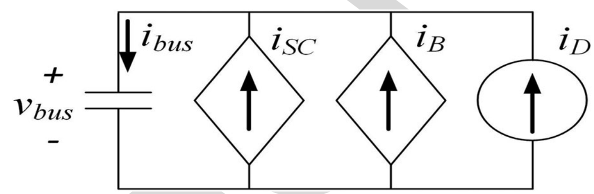

Fig. 4. EMS equivalent circuit for analysis and simulations.

i_{SC}, the battery current i_B, and a disturbance current i_D, which is equal to i_{emsdc} in Fig. 1.

For the equivalent circuit in Fig. 4, the following equations can be written using basic circuit analysis:

$$i_{SC} + i_B + i_D = sCv_{bus}. \quad (3)$$

First, let us analyze the HESS controller, when there is no BPF. This is accomplished by removing the BPF block from Fig. 3 and then rewriting (3) by substituting i_{SC}

$$(v_{bus}^* - v_{bus}) = \left(K_p + \frac{K_i}{s}\right) - i_B + i_B + i_D. \quad (4)$$

From (4), when the disturbance i_D is zero, the dc voltage transfer function can be derived

$$\frac{v_{bus}}{v_{bus}^*}\Big|_{i_D=0} = \frac{sK_p + K_i}{s^2C + sK_p + K_i}. \quad (5)$$

The dc voltage due to the disturbance current, when the reference dc-bus voltage is zero, is

$$\frac{v_{bus}}{i_D}\Big|_{v_{bus}^*=0} = \frac{s}{s^2C + sK_p + K_i}. \quad (6)$$

The dc-bus voltage transfer function v_{bus}/v_{bus}^* and the dc-bus voltage transfer function with the disturbance current as the input v_{bus}/i_D are plotted in Fig. 5.

The gain for v_{bus}/i_D is greater than 1, which will cause a lot of ripple if there is any ac current present in the disturbance current. The second harmonic current flowing from the dc bus to the ac load is significant and causes dc-bus ripple. This problem can be mitigated by adding a BPF to identify and close a control loop on the second harmonic voltage error.

In contrast to the previous analysis, let us analyze the complete HESS shown in the block diagram of Fig. 3. With the BPF, the dc voltage transfer function becomes

$$\frac{v_{bus}}{v_{bus}^*}\Big|_{i_D=0} = \frac{s^3K_p + s^2K_2 + sK_1 + \delta K_i}{s^4C + s^3K_3 + s^2(K_2 + \delta C) + sK_1 + \delta K_i} \quad (7)$$

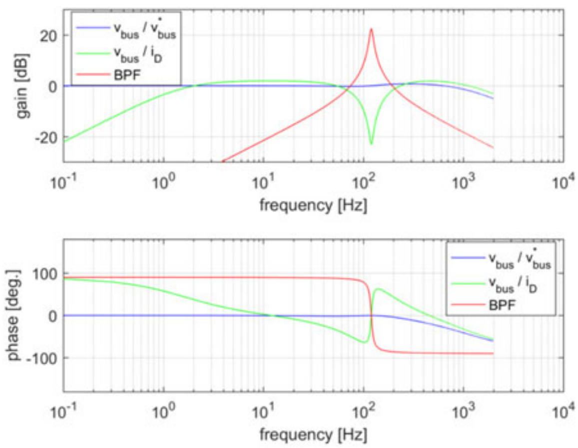

Fig. 5. Bode plots of the transfer functions (5) and (6) without the BPF.

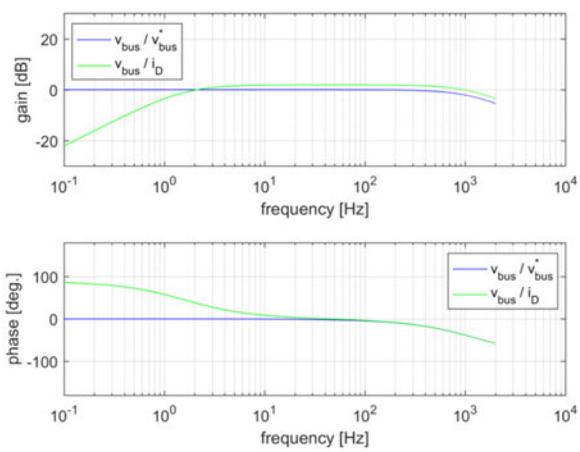

Fig. 6. Bode plots of the transfer functions (7) and (8) with the BPF.

and the dc voltage due to the disturbance current is

$$\frac{v_{\text{bus}}}{i_D}\Big|_{v^*_{\text{bus}}=0} = \frac{s^3 + \kappa s^2 + \delta s}{s^4 C + s^3 K_3 + s^2 (K_2 + \delta C) + s K_1 + \delta K_i}. \tag{8}$$

The coefficients for the transfer functions (7) and (8) are

$$K_1 = \delta K_p + \delta K_i \tag{9}$$

$$K_2 = \kappa K_p + \delta K_i + \beta \tag{10}$$

$$K_3 = \delta K_p + \kappa C. \tag{11}$$

Fig. 6 shows the Bode plots of the transfer functions (7) and (8), where the BPF was added to the control architecture. In contrast with Fig. 5, it can be observed that the addition of the BPF reduces the second harmonic voltage ripple in the dc bus. The BPF has very high gain at 120 Hz, and it reduces the transfer function v_{bus}/i_D significantly at 120 Hz. The BPF has a minimal effect on the transfer function $v_{\text{bus}}/v^*_{\text{bus}}$.

A time-domain simulation of the system represented in Fig. 1 is shown in Fig. 7. The 120-Hz component of the dc-bus ripple is reduced by the BPF. Also, as shown in Fig. 7, the step response to an increase in the dc load current is reduced. The disturbance current used in the simulation of Fig. 7 is a 10-A sinewave at

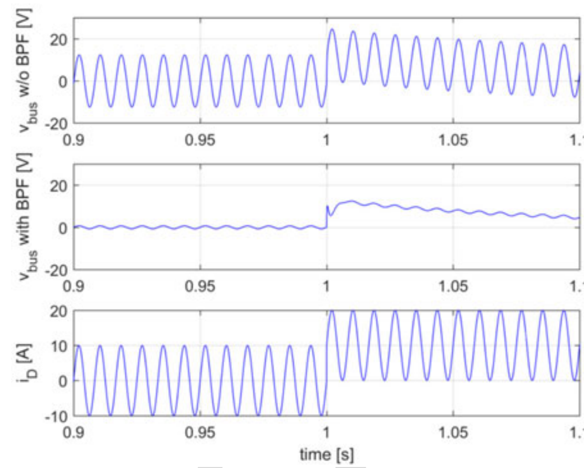

Fig. 7. Time-domain behavior of the HESS controller with and without the BPF for an injected disturbance current i_D (v_{bus} error is shown here).

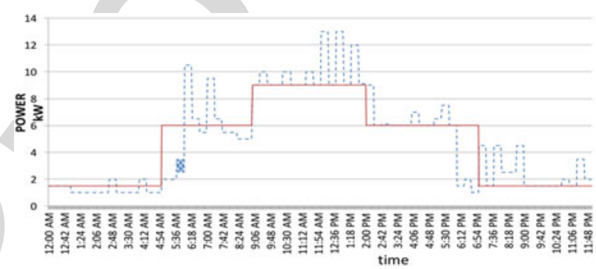

Fig. 8. Load power consumption profile of a remote microgrid, real (DASHED) versus linearized (SOLID) (2-min resolution).

120 Hz plus a 10-A step change in the load current at $t = 1$ s

$$i_D(t) = 10u(t-1) + 10\sin(2\pi 60 t). \tag{12}$$

IV. Lifetime Extension and Economics of an Optimized HESS

In this section, the proposed HESS is used in a remote military microgrid to demonstrate how the above control increases the battery lifetime compared to the same microgrid, where only batteries are used for energy storage. A HESS shows its potential when sudden spikes, not negligible because of the same order of magnitude than the base load, occur. The analysis in this section proves that, when the HESS draws the load transient currents from the SCs, the batteries will last longer. The battery lifetime extension is quantified for different values of the low-pass filter coefficient, and the overall microgrid economics is analyzed.

The power profile of Fig. 8 (dashed line) represents the typical daily consumption in a remote military microgrid, where sudden peaks occur and seriously affect the lifetime of the batteries. This profile is used for the following analysis and case study in contrast to the simplified profile (solid) also plotted in Fig. 8 and used for the study reported in [8].

A. A Few Considerations on the Role of the Optimization

Fuel consumption is one of the parameters that are worth minimizing in a remote military microgrid because fuel

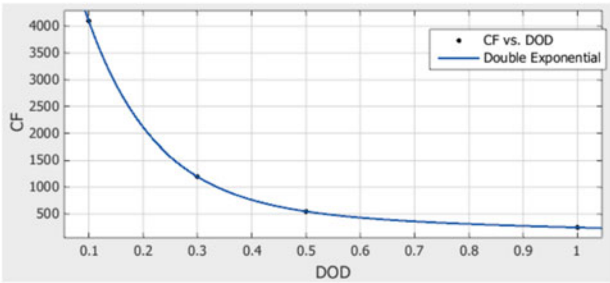

Fig. 9. Reference fitting curve for the lead–acid batteries of the experimental test (CF versus DOD) [26].

transportation to remote sites can result in casualties. In a previous study, the optimization model and its constraints were thoroughly discussed [23]. The results of that optimization are based on 2-min intervals, and it provides the rules for the power sharing among the various sources, taking into account how fast the response from SCs can arrive. These sources include two diesel generators (5 and 15 kW), the PV source (3 kW$_P$, which is deterministic in the proposed example), and the HESS. In addition, the optimization algorithm ensures that the batteries operate within safe SoC limits, and the generators operate within their range of operation and efficiency. The power associated with HESS, P_{HESS}, is thus obtained and is being used in this novel analysis, where the focus is the evaluation of the lifetime of the batteries and the economics of the system, when the controller parameter α varies.

B. Link Between the Controller and the Battery Lifetime

Different battery and SC currents can be obtained by changing the low-pass filter coefficient α, still keeping P_{HESS} constant. With these currents as inputs, we can evaluate the SoC for both devices and find which is the best SoC_* to support the optimized rules

$$\text{SoC}_*(t) = \text{SoC}_*(t-1) - \frac{P_*(t)\Delta t}{\text{ASE}_*}. \tag{13}$$

With SoC_*, P_*, and ASE_*, we identify the SoC, the active power (positive when storage is feeding the load, and negative when is charging), and the storage capacity of each specific device (either the battery or the SCs)

$$P_*(t) = P_{\text{BAT}}(t) = v_{\text{bus}}(t).i_B(t) \text{ but also}$$

$$P_*(t) = P_{\text{SC}}(t) = v_{\text{bus}}(t).i_{\text{SC}}(t) \tag{14}$$

$$P_{\text{HESS}}(t) = P_{\text{BAT}}(t) + P_{\text{SC}}(t). \tag{15}$$

The currents i_B and i_{SC} must have the same sign, or being 0, meaning that when one device is charging or discharging, the other must act accordingly or it must be OFF.

The battery lifetime is thus assessed by using the Rainflow counting method [24], [25], which needs the results of the SoC over time to provide the number and typology of cycles characterizing the charge and discharge of the battery over a typical horizon. Each kind of battery shows its own cycle to failure (CF) versus depth of discharge (DoD). In Fig. 9, such data for the lead–acid batteries used in the laboratory prototype are reported. We recall that the use of lead–acid batteries is due to safety reasons. Nevertheless, this methodology applies to any kind of battery technology, as long as the CF versus DoD curve can be obtained.

The Rainflow counting algorithm provides information on amplitude (related to the DoD) and frequency of cycles presenting the same amplitude on a set time horizon. The life expectancy of the battery is related to the CF, with 1/CF being the life fraction. We can assess D, the inverse of the lifetime, as

$$D = \sum_{i=1}^{m} \frac{N_i}{\text{CF}_i} \tag{16}$$

where m is the number of different DoD_i, occurring in the set horizon, N_i is the frequency associated with DoD_i, and CF_i is the corresponding number of cycles at DoD_i. For a fully functional battery, D has to be less than 1. When $D = 1$, the battery is considered dead; its unit measure depends on how the number of cycles N_i is counted: if N_i are counted over a day, then the lifetime of the battery (inverse of D) counts the days to failure (DF).

An exemplification: if in a typical day, a battery experiences 10 cycles/day (N), where DoD (the amplitude of the equivalent charge/discharge cycle) is equal to 0.2, then that battery can ideally survive for up to 200 equivalent days, before being considered dead. In fact, $\text{CF@}_{\text{DoD}=0.2}$ is 2000; hence, the lifetime in days $1/D = \text{CF}/N = 200$. When multiple cycles occur, the lifetime is the composition of each single assessment. D depends on N, which relates to DoD; DoD depends on SoC_{BAT} and SoC depends on the low-pass filter coefficient α; thus, D depends on α.

To sum up the analysis: the higher α, the less current on SC; thus, the lower the lifetime of the battery. To achieve a certain lifetime, we tune the α value, accordingly.

The overall implemented procedure ensures minimum fuel consumption, while suitably tuning the battery lifetime, at the same time. This last objective is achieved by tuning the HESS controller. In the following subsection, we will show how α will also affect the HESS investments and its economics.

C. Case Study Results

In Fig. 10, input and output data, from the optimization procedure described in [23], are reported for the case study: a remote military microgrid. Case A is the reference case when storage is made up only by batteries (no SCs), while case B represents the case when the HESS is present (with SCs). The needed data for both cases, regarding the features of the optimized considered system, deal with the battery, the gensets, and the load profile on a set horizon. In particular, for the battery, the parameters are the following:

1) SoC_{min} and SoC_{max};
2) charging/discharging efficiency η;
3) rated power P_{max};
4) discharging/charging time at P_{max};
5) available capacity.

For gensets 1 and 2, the parameters are the rated powers P_{n1} and P_{n2} and the related relationships between the load factor

	Description	Case B	Case A (Reference)	unit measure	note or symbol
battery	state of charge: range	**0.5-1**	**0.2-1**	p.u	SoC min-max values
		SoC(t=0)=SoC(t=end of the day)			typical day assumption
	charge/ discharge efficiency	0.9/0.9	0.9/0.9	p.u.	
	maximum available constant battery power (rated)	3	3	kW	Pbat max
	duration time @ Pbat max	6	6	hours	T
	Battery capacity	18	18	kWh	ASE
genset	rated power	5-15	5-15	kW	P1n, P2n
general parameters	a total of 720 t per typical day	2	2	minutes	t step
	Load in a typical day	Fig.8	Fig. 8	W	PL
results	power from/to the storage	Phess =200*(iB+ iSC)	Pbat= 200*iB	W	
	power shares among sources	Fig.14	Fig.11		

Fig. 10. Matrix visualization of all the most important input and output information coming from the previous optimization.

and the fuel consumption [8]. Furthermore, the time step t and the load profile P_L shall be established.

Also, Fig. 10 reports in the last row the indication to the resulting output, the balancing of powers to feed the load, meaning the sequence of powers from gensets and to/from the storage unit.

Additionally, for case B, in Table II, technical data of the used basic SC module are reported.

When the DASHED load profile of Fig. 8 is considered for a typical day, the optimized procedure identifies the best $P_{\text{HESS}}(t)$ (or P_{BAT} if no SCs are present) for each time step of the day and for the given conditions.

For case B, we consider three scenarios, cases B1, B2, and B3, identified by different values of the low-pass filter coefficient α, equal to 0.005 (B1), 0.003 (B2), and 0.001 (B3). Once the optimization has produced the power share among the gensets and the storage, then different alphas determine a different sequence for $i_B^{B1,B2,B3}(t)$ and $i_{\text{SC}}^{B1,B2,B3}(t)$ and thus $\text{SoC}_B^{B1,B2,B3}(t)$: superscripts identify the respective scenarios. Similarly, when no SCs are considered, then we will have $i_B^A(t)$ and $\text{SoC}^A(t)$.

TABLE II
SC MAXWELL DATA [27]

Product name	BMOD0130P056 B03
Rated Capacity (F)	130
Rated Voltage (V)	56
ESR (mΩ)	8.1
Leakage current (mA)	120
Absolute maximum current (A)	1,900
max continuous current (A)	61 $\div$ 99
Weight (kg)	18
Stored Energy (Wh)	56.6
$P_{\text{SC}_{\max}}$ (kW)	96.79
t @ $P_{\text{SC}_{\max}}$ (s)	2.11
cost of single unit ($)	1,300

TABLE III
CASE STUDY: MAIN RESULTS FOR THE THREE SCENARIOS (B1, B2, AND B3) AND THE REFERENCE CASE A

Description↓	$\alpha\rightarrow$	**0.005** B1	**0.003** B2	**0.001** B3	**Ref.** case A
SCs capacitance	F	650	910	1300	no SC
set $\text{SoC}_{\min}$		0.5	0.5	0.5	**0.2**
The lowest SoC	%	69.9	67.53	67.06	**30**
Cycles		20	18	16	**51**
Lifetime	days	274	282	363	**122**
Invest. on SC	k$	6.5	9.1	13	N.S.
Invest. on BAT.	k$	10.8	10.8	9.	**25.2**
Tot. Inv. (5y)	k$	17.3	19.9	22.	**25.2**

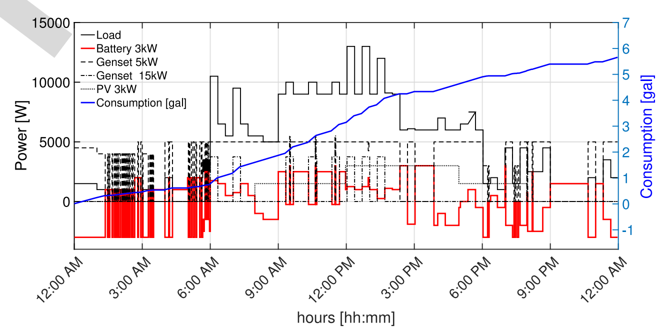

Fig. 11. Case A (only with batteries): from the optimization [23]: power profile and consumption (resolution step 2 min; $\text{SoC}_{\min} = 0.2$).

For each of the four SoC sequences, a new series of $\text{DoD}^{B1,B2,B3,A}$ is derived, and different lifetimes are expected.

In Table III, the main results are reported for the three scenarios [increasing SCs number from 5 (B1) to 10 (B3)], after the optimization and the tuning of α, as well as for the Reference case A, optimized but without SCs.

The investment (INV^i) in each ith scenario/case is thus evaluated as in the following, depending on the DF of the batteries, which ultimately depends on alpha:

$$\text{INV}^i\left(\text{DF}\left(\alpha\right)\right) = \text{INV}_{\text{SC}}^i + \sum_{\text{DF}} \text{INV}_B^i\left(\text{DF}\left(\alpha\right)\right). \quad (17)$$

The change in i_B and i_{SC} sequences can be visualized when simulating the battery current with and without SCs. In Figs. 11

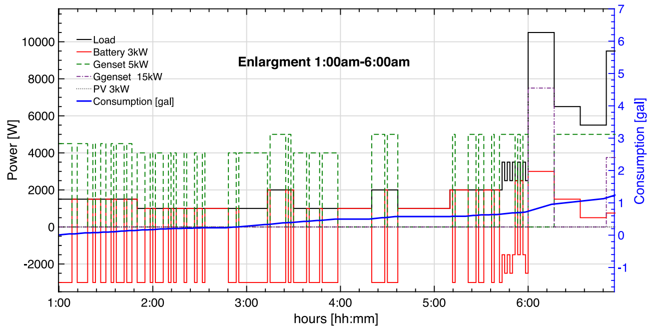

Fig. 12. Case A: Enlargement between 1:00 A.M. and 6:00 A.M. (resolution step 2 min; $\mathrm{SoC_{min}} = 0.2$).

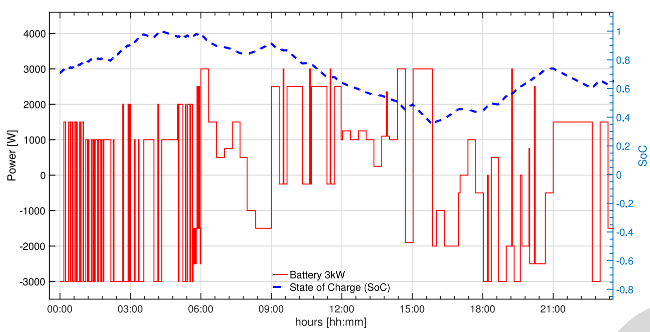

Fig. 13. Case A: Optimal P_{BAT} and consequent SoC on batteries (resolution step 2 min; $\mathrm{SoC_{min}} = 0.2$).

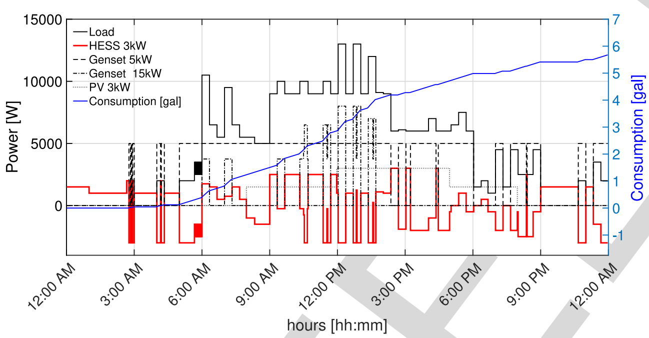

Fig. 14. Case B (with the HESS): from the optimization [23]: power profile and consumption (resolution step 2 min; $\mathrm{SoC_{min}} = 0.5$) .

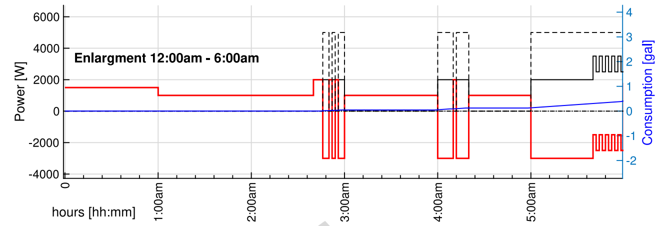

Fig. 15. Case B: Enlargement between 1:00 A.M. and 6:00 A.M. (resolution step 2 min; $\mathrm{SoC_{min}} = 0.5$).

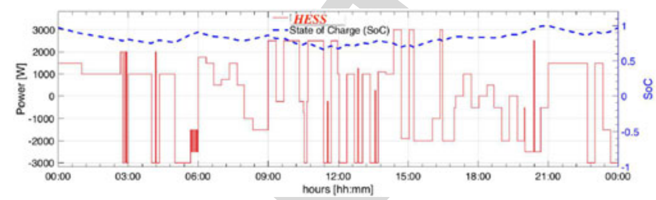

Fig. 16. Case B: Optimal P_{HESS} and consequent SoC on batteries (resolution step 2 min; $\mathrm{SoC_{min}} = 0.5$).

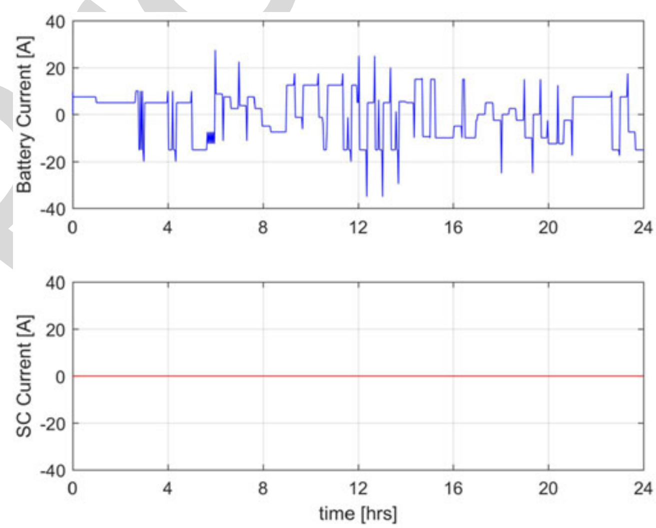

Fig. 17. Case B: battery current when the HESS control system is in place but is disabled (with transient, resolution step 0.1 s). SC current is zero.

and 14, the optimization results are reported for case A (Reference) and for case B: what is referred as HESS profile is the active power associated with what is coming from/to the storage unit (no transient considered, resolution step 2 min).

For a better understanding of the battery dynamic, in terms of charging/discharging cycles and consequent SoC, Figs. 12 and 13 for case A and Figs. 15 and 16 for case B are reported.

They show an enlargement of Figs. 11 and 14, respectively, when SCs are not included (case A) and when they are included (case B).

A Simulink model produced the simulated plots in Figs. 17–19. Omitting the switching behavior of the EMS power converters lead to shorter simulation times for the battery current over a 24-h period (resolution 0.1 s). In Fig 17, the battery current is plotted (upper), when yet the SCs are to be turned ON, the transient is considered, and the resolution step is 0.1 s. In Figs. 18 and 19, battery and SC currents are shown, respectively, when the HESS controller is operational with the low-pass filter coefficient $\alpha = 0.005$ (B1) and $\alpha = 0.001$ (B3). It can be observed that the battery current is much smoother when the HESS controller is used to redirect the peak currents to the SCs, and we can also notice how the α value affects the i_B profile (upper graph of Figs. 17–19).

In Fig. 20 (Scenario B1) and Fig. 21 (Scenario B3), the battery cycles are reported for α equal to 0.005 (smaller SCs) and 0.001 (bigger SCs). The main results are reported in Table III, where the increase in DF (122 estimated days with no SCs, 274 for α = 0.005 up to 363 for $\alpha = 0.001$), the assessment of the lowest SoC, and investments are assessed with respect to the illustrated procedure.

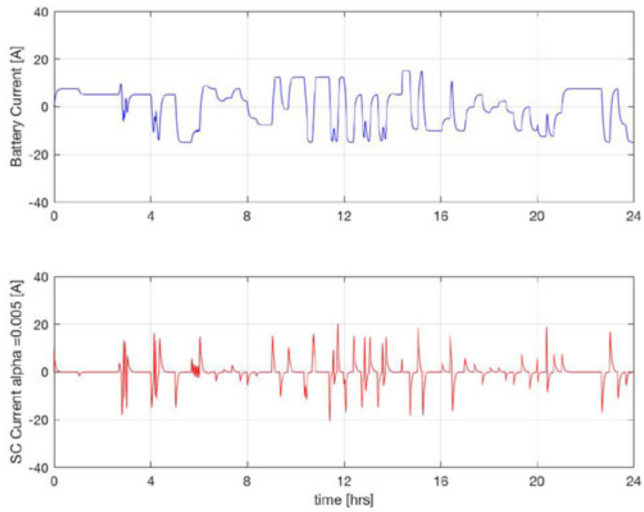

Fig. 18. Scenario B1: battery and SC current when the HESS control system is enable. SCs takes the peaks of the load current (α=.005, resolution step 0.1 s).

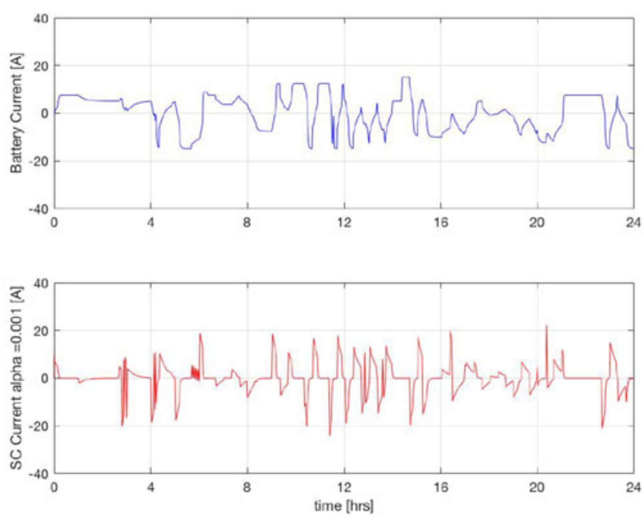

Fig. 19. Scenario B3: battery and SC current with the HESS control system. SCs take the peaks of the load current ($\alpha = 0.001$, resolution step 0.1 s).

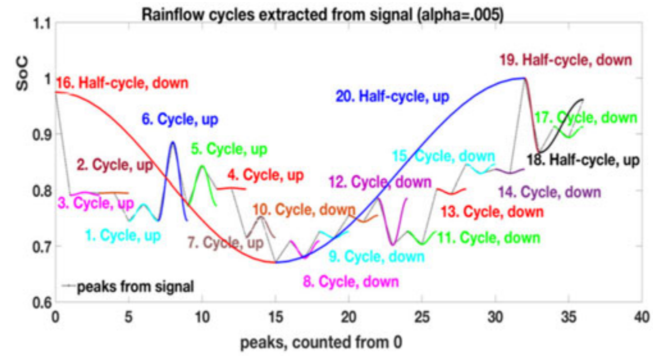

Fig. 20. Scenario B1: Counting cycles at different DoD ($\alpha = 0.005$).

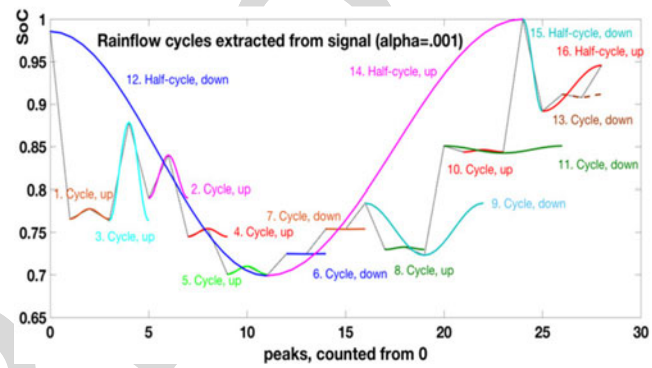

Fig. 21. Scenario B3: Counting cycles at different DoD ($\alpha = 0.001$).

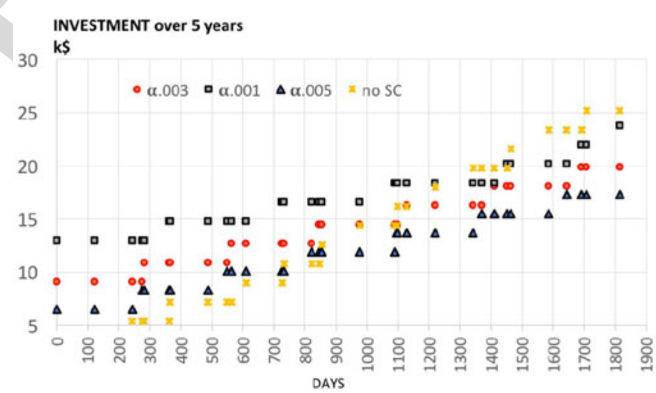

Fig. 22. Investment over five years ($\alpha = 0.005$ blue triangle; $\alpha = 0.003$ orange circle; $\alpha = 0.001$ gray square; yellow star = Reference—NO SCs).

The plots in Fig. 22 and the results in Table III demonstrate how the battery lifetime is extended when the HESS controller is used, realizing the least investment over five years, when α is lower, thus finding the suitable tradeoff between increasing SCs size and the battery wearing out. We can also notice that below ∽900 operating days, even only five SCs modules are not convenient against batteries, but above 900 days, the HESS becomes cost effective. Over ∽1500 days, every investigated HESS is more cost effective than batteries alone.

Depending on the size of the SC and batteries, thus on the deriving cycles to failure, we can infer that the daily power consumption is a key parameter for the economic evaluation. Therefore, careful microgrid load analysis should be done to create a reliable load profile. A sensitivity analysis can also be performed to identify not only the actual optimum, but also the proper range of validity for the current assessment and link it to the controller parameters. This will be illustrated in a future work.

Our methodology makes easily evident how those battery technologies with higher CF versus DoD (for instance, the lithium ones) can positively affect the lifetime assessment because higher CF values directly influence (16). On the other hand, they cost more; thus, again, another sensitivity analysis, focusing on prices, can help in investigating how far our considerations can be stretched.

V. Experimental Measurements

To verify the functionality of the proposed HESS controller, a laboratory experiment was conducted with a scaled-down EMS prototype. The laboratory setup is represented in Fig. 23, where the EMS is included inside the blue box. Note that instead of

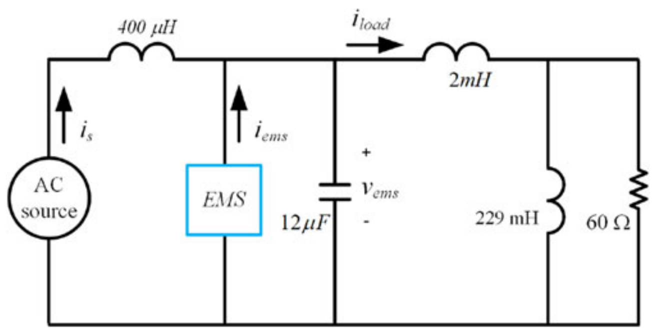

Fig. 23. Schematic of the laboratory setup for the experimental validation.

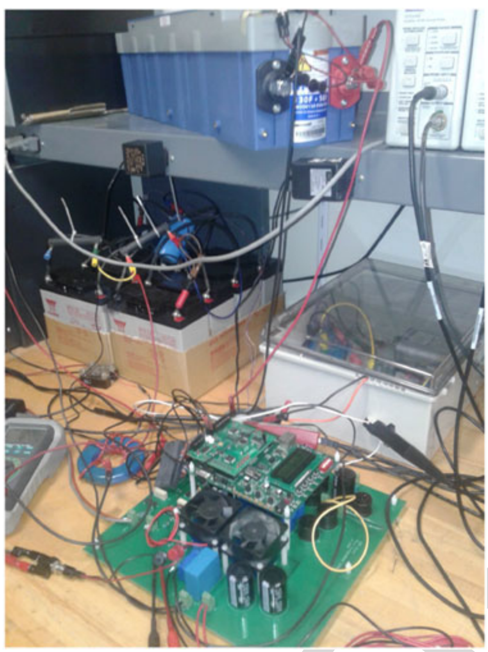

Fig. 24. Photograph of the laboratory setup.

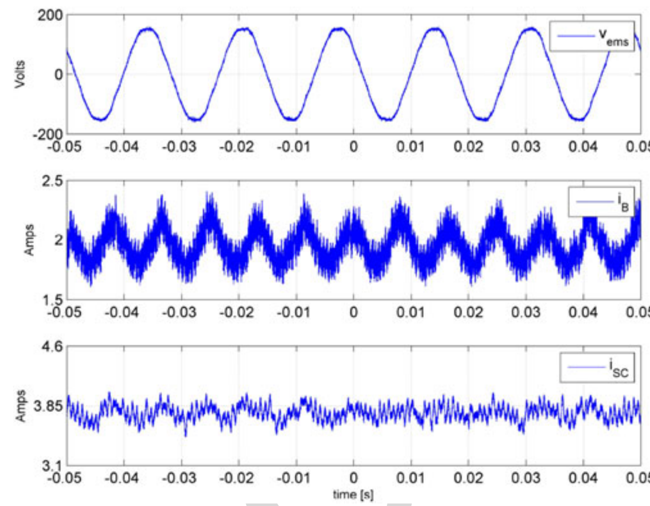

Fig. 25. Case B without HESS controller steady-state experimental waveforms. From the top: ac voltage, battery current, and SC current.

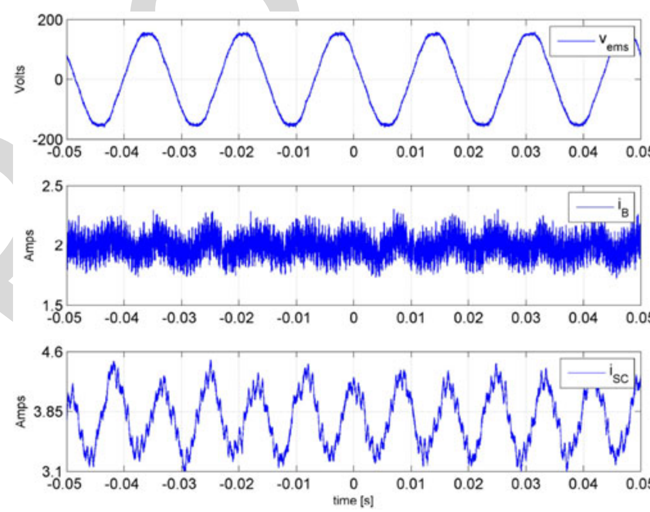

Fig. 26. Case B with HESS controller steady-state experimental waveforms. From the top: ac voltage, battery current, and SC current.

a diesel generator, the ac 120-V 60-Hz power available in the laboratory was used.

A photograph of the prototype on the laboratory bench is shown in Fig. 24. A 130-F Maxwell SC [27] and six Genesis 12-V lead–acid batteries [26] connected in series are visible in the photograph, together with the EMS hardware, which includes several printed circuit boards (PCBs) and external passive components. The EMS controller is embedded on an FPGA, which is part of a Xilinx developed board [28]. The other PCBs are custom made, with the bottom one comprising the power electronics and passive components and the top PCB including A/D converters, USB interface to communicate with a personal computer, and other electronic components that interface with the FPGA board. The code for the FPGA is developed in Simulink with the additional Xilinx System Generator [29] blocks. Further details of the EMS hardware and FPGA software implementation are available in [7] and [9].

The first set of experiments produced the steady-state plots in Figs. 25 and 26 with an without the proposed HESS controller, respectively. The two figures include, from the top, the ac source voltage, the battery current, and the SC current. The contrast between the battery current in Fig. 25 and the battery current in Fig. 26 validates the effectiveness of the HESS controller in removing the 120-Hz frequency component from the battery and sending it to the SC. Harmonic analysis of the battery current from Fig. 25 shows that the amplitude of the 120-Hz harmonic is 158 mA. In contrast, the 120-Hz harmonic of i_B in Fig. 26 is 45.5 mA, a substantial reduction.

A second set of experiments is shown in Figs. 27 and 28, where the dynamic performance of the system is contrasted without and with the HESS controller, respectively. As discussed in previous sections, in order to reduce the charge and discharge cycles on the batteries, the SC is commanded to absorb or deliver currents that are suddenly needed by the microgrid. One example is just before 3:00 P.M. (or 15:00 hours; see Fig. 14); when a large amount of energy is being sent to the HESS and, as shown in Fig. 18, the SC absorbs the initial peak. Fig. 27 demonstrates

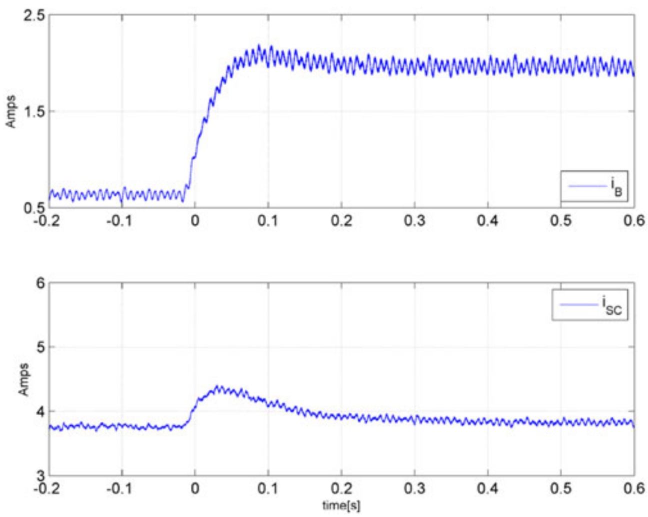

Fig. 27. Battery charge current increase from 1 to 2 A without the HESS controller. Upper i_B and lower i_{SC}.

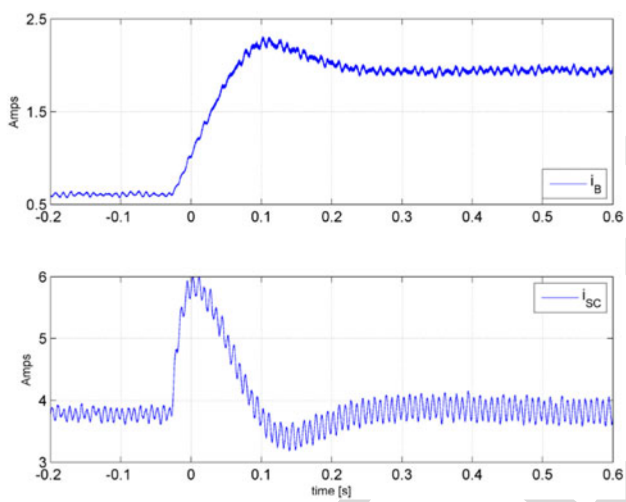

Fig. 28. Battery charge current increase from 1 to 2 A with the HESS controller. Upper i_B and lower i_{SC}.

what happens when the current sent to the battery is doubled from 1 to 2 A: the surge is evident in the battery current, i_B, as well as the 120-Hz ripple. In contrast, the *di/dt* on the battery current i_B is reduced when the HESS controller is turned ON, and also, its ripple is noticeably reduced. Note that $\alpha = 5\,\text{Hz}$ for this experiment.

VI. Conclusion

This paper presents a novel HESS controller focused on increasing the lifetime of the batteries by using SCs with a buck–boost converter to control their charge and discharge, thus maximizing their utilization. A realistic load profile is used, and several scenarios are compared to link the controller parameter α with the battery lifetime extension and to the economic evaluations. Therefore, the economic evaluation is performed on a five-year period, time needed to show when the HESS may become cost effective for the case study. The SCs are sized to take the stress off the load power transients from the battery pack, so that the batteries only "see" an idealized load profile and can perform at better conditions.

Experimental measurements demonstrate the ability of the proposed HESS controller to suppress the 120-Hz ripple from the battery as well as reduce the di/dt when higher currents are commanded. This result proves that the HESS controller redirects higher frequency currents to the SC and leave for the batteries only slow current changes in order to increase the battery lifetime.

Future work will focus on optimizing the number of SCs in order to reduce their economic impact on the microgrid.

Acknowledgment

The authors are grateful to V. Catania for his help with the SC verification and the preceding optimization.

References

[1] G. Quartarone, M. Liserre, F. Fuchs, N. Anglani, and G. Buticchi, "Impact of the modularity on the efficiency of smart transformer solutions," in *Proc. 40th Annu. Conf. IEEE Ind. Electron. Soc.*, 2014, pp. 1512–1518.

[2] J. Rocabert, A. Luna, F. Blaabjerg, and P. Rodríguez, "Control of power converters in ac microgrids," *IEEE Trans. Power Electron.*, vol. 27, no. 11, pp. 4734–4749, Nov. 2012.

[3] A. A. Ferreira, J. A. Pomilio, G. Spiazzi, and L. de Araujo Silva, "Energy management fuzzy logic supervisory for electric vehicle power supplies system," *IEEE Trans. Power Electron.*, vol. 23, no. 1, pp. 107–115, Jan. 2008.

[4] H. Kanchev, D. Lu, F. Colas, V. Lazarov, and B. Francois, "Energy management and operational planning of a microgrid with a PV-based active generator for smart grid applications," *IEEE Trans. Ind. Electron.*, vol. 58, no. 10, pp. 4583–4592, Oct. 2011.

[5] R. Kelly, G. Oriti, and A. Julian, "Reducing fuel consumption at a remote military base: Introducing an energy management system." *IEEE Electrific. Mag.*, vol. 1, no. 2, pp. 30–37, Dec. 2013.

[6] N. R. Tummuru, M. K. Mishra, and S. Srinivas,"Dynamic energy management of renewable grid integrated hybrid energy storage system," *IEEE Trans. Ind. Electron.*, vol. 62, no. 12, pp. 7728–7737, Dec. 2015.

[7] G. Oriti, A. Julian, and N. Peck, "Power-electronics-based energy management system with storage," *IEEE Trans. Power Electron.*, vol. 31, no. 1, pp. 452–460, Jan. 2016.

[8] N. Anglani, G. Oriti, and M. Colombini, "Optimized energy management system to reduce fuel consumption in remote military microgrids," *IEEE Trans. Ind. Appl.*, vol. 53, no. 6, pp. 5777–5785, Nov./Dec. 2017.

[9] G. Oriti, A. Julian, N. Anglani, and G. Hernandez, "Novel hybrid energy storage control for a single phase energy management system in a remote islanded microgrid," in *Proc. IEEE Energy Convers. Congr. Expo.*, Oct. 2017, pp. 1–8.

[10] A. M. van Voorden, L. M. R. Elizondo, G. C. Paap, J. Verboomen, and L. van der Sluis, "The application of super capacitors to relieve battery-storage systems in autonomous renewable energy systems," in *Proc. IEEE Lausanne Power Tech*, Jul. 2007, pp. 479–484.

[11] J. M. Blanes, R. Gutiérrez, A. Garrigós, J. L. Lizán, and J. M. Cuadrado, "Electric vehicle battery life extension using ultracapacitors and an FPGA controlled interleaved buck-boost converter," *IEEE Trans. Power Electron.*, vol. 28, no. 12, pp. 5940–5948, Dec. 2013.

[12] B. Hredzak, V. G. Agelidis, and M. Jang, "A model predictive control system for a hybrid battery-ultracapacitor power source," *IEEE Trans. Power Electron.*, vol. 29, no. 3, pp. 1469–1479, Mar. 2014.

[13] D. B. W. Abeywardana, B. Hredzak, and V. G. Agelidis, "Battery-supercapacitor hybrid energy storage system with reduced low frequency input current ripple," in *Proc. Int. Conf. Renew. Energy Res. Appl.*, Nov. 2015, pp. 328–332.

[14] D. B. W. Abeywardana, B. Hredzak, V. G. Agelidis, and G. D. Demetriades, "Supercapacitor sizing method for energy-controlled filter-based hybrid energy storage systems," *IEEE Trans. Power Electron.*, vol. 32, no. 2, pp. 1626–1637, Feb. 2017.

[15] W. Wei and W. Ping, "A novel power decoupling technique for single-phase photovoltaic grid-connected inverter," in *Proc. 5th Int. Conf. Power Electron. Syst. Appl.*, Dec. 2013, pp. 1–6.

[16] A. M. Gee, F. V. P. Robinson, and R. W. Dunn, "Analysis of battery lifetime extension in a small-scale wind-energy system using supercapacitors," *IEEE Trans. Energy Convers.*, vol. 28, no. 1, pp. 24–33, Mar. 2013.

[17] H. Zhou, T. Bhattacharya, D. Tran, T. Siew, and A. Khambadkone, "Composite energy storage system involving battery and ultracapacitor with dynamic energy management in microgrid applications," *IEEE Trans. Power Electron.*, vol. 26, no. 3, pp. 923–930, Mar. 2011.

[18] S. K. Kollimalla, M. K. Mishra, and N. L. Narasamma, "Design and analysis of novel control strategy for battery and supercapacitor storage system," *IEEE Trans. Sustain. Energy*, vol. 5, no. 4, pp. 1137–1144, Oct. 2014.

[19] W. Jiang, L. Zhang, H. Zhao, H. Huang, and R. Hu, "Research on power sharing strategy of hybrid energy storage system in photovoltaic power station based on multi-objective optimisation," *IET Renew. Power Gener.*, vol. 10, no. 5, pp. 575–583, 2016.

[20] V. I. Herrera, H. Gaztañaga, A. Milo, A. S. de Ibarra, I. Etxeberria-Otadui, and T. Nieva, "Optimal energy management and sizing of a battery-supercapacitor-based light rail vehicle with a multiobjective approach," *IEEE Trans. Ind. Appl.*, vol. 52, no. 4, pp. 3367–3377, Jul./Aug. 2016.

[21] A. Tani, M. B. Camara, and B. Dakyo, "Energy management in the decentralized generation systems based on renewable energy, ultracapacitors and battery to compensate the wind/load power fluctuations," *IEEE Trans. Ind. Appl.*, vol. 51, no. 2, pp. 1817–1827, Mar./Apr. 2015.

[22] J. Aguado, A. J. Sanchez-Racero, and S. de la Torre, "Optimal operation of electric railways with renewable energy and electric storage systems," *IEEE Trans. Smart Grid*, vol. 9, no. 2, pp. 993–1001, Mar. 2018.

[23] N. Anglani, G. Oriti, A. Julian, and V. Catania, "How to control supercapacitors and to account for the consequent extension of battery lifetime in an isolated ac microgrid," in *Proc. IEEE Int. Conf. Environ. Elect. Eng./IEEE Ind. Commercial Power Syst. Eur.*, Jun. 2017, pp. 1–6.

[24] S. Downing and D. Socie, "Simple rainflow counting algorithms," *Int. J. Fatigue*, vol. 4, no. 1, pp. 31–40, Jan. 1982. [Online]. Available: http://www.sciencedirect.com/science/article/pii/0142112382900184

[25] A. Nieslony, MATLAB central-rainflow counting algorithm, 2010. [Online]. Available: http://scholar.google.it/scholar?hl=it&q=adam+nieslony+Rainflow+Counti ng+Algorithm&btnG=&lr=#2

[26] Genesis 150 NP12-12 batteries—specifications. [Online]. Available: http://datasheet.octopart.com/NP12-12-EnerSys-datasheet-10655.pdf. Accessed on: Jun. 5, 2018.

[27] All ultracapacitor Maxwell documents, Nov. 2017. [Online]. Available: http://www.maxwell.com/products/ultracapacitors/downloads

[28] "Xilinx® 'Avnet Virtex-4 LC development board'," Feb. 2018. [Online]. Available: http://www.xilinx.com/products/devkits/DS-KIT-4VLX25LC.htm

[29] *System Generator for DSP—Getting Started Guide*, release 10.1, Xilinx, San Jose, CA, USA, Mar. 2008.

Giovanna Oriti (S'94–M'97–SM'04) received the Laurea (Hons.) and Ph.D. degrees in electrical engineering from the University of Catania, Catania, Italy, in 1993 and 1997, respectively.

She was a Research Intern with the University of Wisconsin, Madison, for two years. After graduation, she joined the United Technology Research Center, where she developed innovative power converter topologies and control. In 2000, she launched her own consulting business developing physics-based models of power converters and drives for electromagnetic interference analysis, stability analysis, and development of control algorithms. In April 2008, she joined the faculty of the Electrical and Computer Engineering (ECE) Department, Naval Postgraduate School (NPS), Monterey, CA, USA, where she is currently a tenured Associate Professor. She holds one U.S. patent and has coauthored 50 papers published in IEEE Transactions or IEEE conference proceedings. Her research interests include power electronic converters for electric ship systems, energy management, microgrids, and renewable energy interface.

Dr. Oriti was the Chair of the Industrial Power Conversion System Department of the IEEE Industry Application Society (IAS) in 2011–2012. She was the recipient of the 2002 IEEE IAS Outstanding Young Member Award. In 2012, she was the recipient of the NPS ECE Service Award in recognition of her contribution to the development of the new NPS EE Energy curriculum. In 2016 and 2017, she was the recipient of the NPS ECE Research Award in recognition of her contributions, through her research, to the U.S. Navy's goal of energy efficiency.

Alexander L. Julian (S'91–M'98–SM'xx) received the B.S.E.E. and M.S.E.E. degrees from the University of Missouri, Columbia, MO, USA, in 1991 and 1992, respectively, and the Ph.D. degree in electrical engineering from the University of Wisconsin–Madison, Madison, WI, USA, in 1998.

After working for two years at the United Technologies Research Center, developing novel power converters for different industrial applications, he contributed to shipboard electronic designs and research for many years as a consultant to Navy vendors by designing, modeling, and prototyping power electronics and motion control systems. From 2004 to 2017, he was a faculty member of the Department of Electrical and Computer Engineering, Naval Postgraduate School, Monterey, CA, USA, being awarded Tenure in 2011. He is currently a consultant. He holds four U.S. patents and has coauthored more than 40 papers in IEEE Transactions or IEEE conference proceedings. His research interests include solid-state power converter design and control, motor drives, electromagnetic interference, reliability and stability analysis for distributed power systems, power converters for renewable energy interface, and microgrids.

Norma Anglani (S'93–M'99) received the Laurea (Hons.) and Ph.D. degrees in electrical engineering from the University of Pavia, Pavia, Italy, in 1993 and 1999, respectively.

After graduating, she worked for a consulting company in the energy efficiency area. Later, she was a Postdoctoral Fellow with the Energy Analysis Group and with the Energy Efficiency Standards Group, Lawrence Berkeley National Laboratory, Berkeley, CA, USA. She is currently an Assistant Professor with the Department of Electrical, Computer and Biomedical Engineering, University of Pavia, Pavia, where she currently teaches and does research in the field of energy management, energy planning, modeling, and efficient compressed air systems. She set up the Labac laboratory, a joint effort between academia and industry. She has been responsible for several research contracts with public and private bodies and has coauthored more than 60 scientific papers.

Dr. Anglani has been a Chartered Engineer since 1995.

Gabriel D. Hernandez received the B.S.E.E. degree from the University of California at Davis, Davis, CA, USA, in 2004, and the M.S.E.E. and E.E. degrees from the Naval Postgraduate School, Monterey, CA, in 2016.

As a U.S. Navy Submarine Officer, he has served aboard the submarine USS OHIO (SSGN 726) and is currently an Engineering Duty Officer managing a submarine-engineered overhaul with Portsmouth Naval Shipyard, Kittery, ME, USA.

Novel Economic Analysis to Design the Energy Storage Control System of a Remote Islanded Microgrid

Giovanna Oriti, *Senior Member, IEEE*, Alexander L. Julian, *Senior Member, IEEE*, Norma Anglani, *Member, IEEE*, and Gabriel D. Hernandez

***Abstract*—This paper presents a novel power flow control strategy, combined with an economic analysis, for an energy management system (EMS) involving a hybrid energy storage. The EMS operates a remote microgrid and directs the power flow to either batteries or supercapacitors to increase the life of the batteries. This paper demonstrates how the use of supercapacitors increases the lifetime of the batteries and ultimately how it affects the economics of the system. The proposed EMS controller also compensates for the 120-Hz ripple on the dc bus. Modeling, simulations, and experimental verification are presented together with the procedure to perform the assessment of the battery lifetime, according to the tuning parameters of the controller.**

***Index Terms*—Battery lifetime, energy management, hybrid energy storage, power converters, supercapacitors (SCs).**

I. Introduction

MICROGRID technology has been developed and closely investigated as one of the solutions to increase energy security. Solid-state power converters are instrumental to microgrid operations [1]. Power-electronics-based energy management systems (EMS) have been recently explored (see [2]–[8]) to control loads and distributed energy resources (DERs), to detect grid failure, and to enable the microgrid islanding mode of operation. Although an EMS is sometimes used to define the software or controller that manages the energy in a power system or microgrid, in this paper, it is used to define a system, which includes one or more power converters that interface to a microgrid and different DERs. In addition to the hardware, the EMS includes several layers of control to manage currents and voltages, as well as loads and sources. An EMS has been recently proposed to optimize operations in remote military microgrids, where continuous service to critical power loads is essential [5], [8]. In this paper, we focus on the EMS ability to control the power flow when a hybrid energy storage system (HESS) is added to the architecture because the real load profile, showing sudden peaks, is considered [9]. The goal of the proposed HESS is to divert the 120-Hz ripple and the peak current ripple away from the batteries by adding supercapacitors (SCs) controlled by a buck–boost converter, thus increasing the lifetime expectation of the batteries available in the microgrid. A novel study to tune the controllers parameters is carried out for a remote military microgrid model. Recent publications [10]–[19] have addressed hybrid storage systems with batteries and SCs in different configurations. Some HESS configurations have used different power converter topologies and controllers [10], [11], [15], or they do not show a thorough analysis of the control system [6]. In [20], the focus is exclusively the energy management of a light rail vehicle; therefore, the power electronics controller is not addressed.

Other HESS do not control the 120-Hz ripple on the dc bus either because they are applied to three-phase systems [16] or because they service loads that are not single-phase ac [12], [21]. Papers [17] and [18] present HESS controllers that are very similar to the one proposed in this paper, but they do not include the battery lifetime analysis nor the application to the economics of a microgrid as they are presented in this paper. In [19], although a similar HESS controller was used, the power management strategy used has a different scope than the one proposed in this paper; losses and state of charge (SoC) of the SCs are weighted to be optimized, but the authors do not quantify how this procedure affects the expectation of battery lifetime extension. In [22], an interesting application of optimal power flow problem with the HESS is considered, but time steps are bigger (30 s versus our 0.1 s), and no consideration on investments is included: the economic is based on the cost of the saved energy, thus neglecting the role of sizing, which we show is also a key issue when dealing with the HESS. Here, we evaluate how the different controller strategies, implemented with a proper number of SCs, can increase the battery lifetime.

Manuscript received November 27, 2017; revised March 4, 2018; accepted June 7, 2018. Paper 2017-SECSC-1138.R1, presented at the 2017 IEEE Energy Conversion Congress and Exposition, Cincinnati, OH, USA, Oct. 1–5, and approved for publication in the IEEE Transactions on Industry Applications by the Renewable and Sustainable Energy Conversion Systems Committee of the IEEE Industry Applications Society. This work was supported in part by the U.S. Office of Naval Research as part of the Energy Systems Technology Evaluation Program. *(Corresponding author: Norma Anglani.)*

G. Oriti is with the Naval Postgraduate School, Monterey, CA 93943 USA (e-mail: goriti@nps.edu).

A. L. Julian was with the Naval Postgraduate School, Monterey, CA 93943, USA. He is now a consultant in Seaside, CA, USA (e-mail: alexander.julian@ieee.org).

N. Anglani is with the University of Pavia, 27100 Pavia, Italy (e-mail: nanglani@unipv.it).

G. D. Hernandez is an Engineering Duty Officer with Portsmouth Naval Shipyard, Kittery, ME 03904 USA (e-mail: gabe.hernandez@live.com).

Color versions of one or more of the figures in this paper are available online at http://ieeexplore.ieee.org.

Digital Object Identifier 10.1109/TIA.2018.2853041

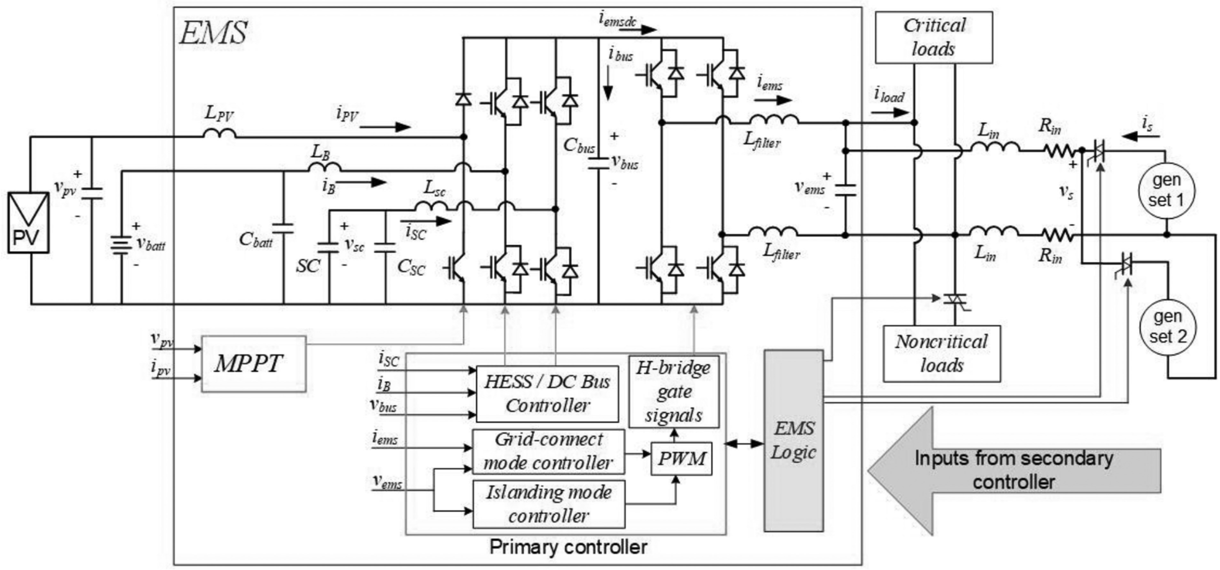

Fig. 1. EMS architecture and its connection to a remote military microgrid with two diesel generators, hybrid energy storage, and PV panels.

To the knowledge of these authors, the proposed combination of a buck–boost converter, a control architecture, and a tight link with the battery lifetime presented in this paper has not been previously presented. Furthermore, the application to a remote microgrid introduces peculiarities in the economics of the considered case study. In this paper, the EMS architecture is presented in Section II. The proposed HESS controller is described in Section III. In Section IV, the procedure, involving the battery lifetime and its link with a specific controller parameter, is presented for a typical power profile of a remote military microgrid. Experimental measurements and conclusions are reported in Sections V and VI, respectively.

II. EMS Functionality and Microgrid Setup

A schematic of the EMS' architecture is provided in Fig. 1 together with the remote military microgrid power system. Also shown in Fig. 1 are critical and noncritical loads and two diesel generator sets (gensets). Critical loads are those loads, including computers, radars, and some air conditioning systems, which are critical to the military operations success and must be powered at all times. Thus, they are hard wired to the ac power bus, while noncritical loads are connected to the ac bus through a solid-state switch controlled by the EMS to enable shedding when necessary. In this setup, the noncritical loads are grouped together for ease of laboratory demonstration; however, an EMS can control multiple noncritical load switches.

The EMS consists of five inverter legs, a field-programmable gate array (FPGA)-based control system, photovoltaic (PV) panels, battery pack, and SCs. Lead–acid batteries are used for the work presented in this paper; however, any other type of battery could be used, and this is true as far as the methodology concerns. However, lead–acid batteries are presently the technology of choice in remote military camps because they fail without catching fire, unlike Li-ion batteries. The FPGA-based controller includes the dc-bus voltage controller, the ac-bus voltage control during islanding operations, and the EMS ac current in the grid-connected mode. This paper focuses on a new dc-bus voltage controller, while the ac current and voltage control systems are the same as presented in [7]. The FPGA also houses the controls for the HESS and the energy management logic such as load scheduling and grid connect/disconnect. Two legs of the power module are employed as a single-phase bidirectional H-bridge converter, which can be controlled as a current source to inject power from the battery pack to the microgrid or as a voltage source when the gensets are OFF. The third leg of the power module is operated as a bidirectional buck–boost converter to either charge the battery bank or draw energy from it. The fourth leg of the power module is operated as a bidirectional buck–boost converter to either charge the SCs or draw energy from them. Batteries and SCs form the HESS, which is controlled by the EMS. A fifth inverter leg is used as a boost converter that is the interface to the PV panels.

III. HESS Control System

In this section, the HESS control system architecture is presented, and its functionality is demonstrated with analysis in the frequency-domain as well as time-domain simulations.

A. Controller Architecture and Functionality

The dc-bus voltage is held constant by the HESS controller shown in Fig. 2. In addition to regulating the dc bus, the goal of this controller is to distribute the load current between the battery and the SCs. Specifically, the load current is the current that the EMS injects into the ac bus to supplement the power provided by the generators. The peak current demanded by the loads is provided by the SCs instead of the battery to reduce the ac current stress on the battery. The low-pass filter commands the battery current to be absent of abrupt changes. The bandpass filter (BPF) is added to extract the 120-Hz signal, which has a

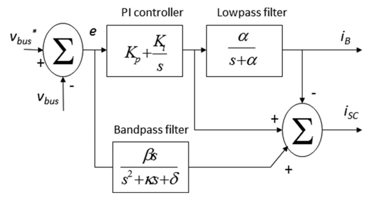

Fig. 2. HESS control system.

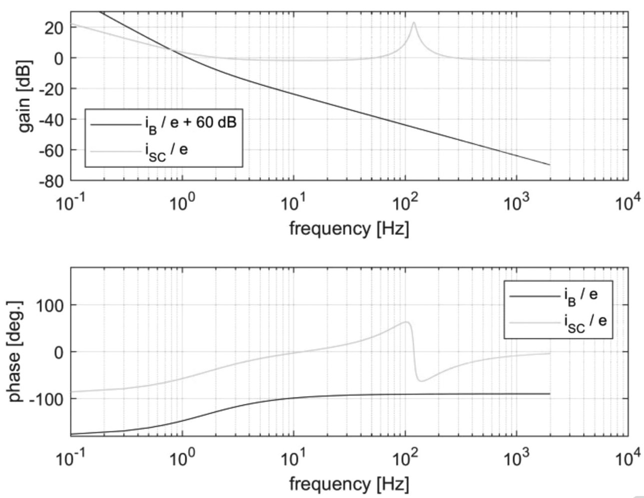

Fig. 3. Bode plots of battery current and SC current transfer functions.

frequency equal to twice the 60-Hz output frequency. The goal of the BPF is to reduce the second harmonic voltage ripple on the dc bus and ac current in the battery. The BPF is analyzed in the next section.

From the control diagram in Fig. 2, the transfer function of the battery current over the dc voltage error can be derived as

$$\frac{i_B}{e} = \frac{\alpha(sK_p + K_i)}{s(s+\alpha)}. \tag{1}$$

The dc voltage error leads to an SC current that is

$$\frac{i_{\text{SC}}}{e} = \frac{(sK_p + K_i)}{s} - \frac{\alpha(sK_p + K_i)}{s(s+\alpha)} + \frac{\beta s}{s^2 + \kappa s + \delta}. \tag{2}$$

The Bode plots of the transfer functions (1) and (2) are shown in Fig. 3. The battery current i_B contains only low-frequency components, while the SCs provide the current for any ac disturbances in the dc bus, especially at 120 Hz. In fact, the top plot in Fig. 3 shows that the gain of the transfer function (2) is high at 120 Hz. The parameters used for this analysis are shown in Table I.

B. Contribution and Analysis of the BPF

It is well known that a 120-Hz component is drawn from the dc bus by a single-phase inverter delivering 60-Hz ac power, so that pulsating power flows from the dc bus in addition to dc power. The role of the BPF in Fig. 3 is to ensure that the 120-Hz current is drawn from the SCs, not the batteries. The following analysis clarifies the contribution of the BPF.

The equivalent circuit in Fig. 4 represents the currents that are flowing to/from the EMS dc bus, which are the SC current

TABLE I
PARAMETERS OF THE CONTROLLER

Description	Symbol	Value
DC bus capacitor	C_{bus}	100 μF
Proportional gain	K_p	0.8
Integral gain	K_i	8
BPF coefficient	β	754
BPF coefficient	κ	57
BPF coefficient	δ	568,000
Low-pass filter coefficient	α	0.005 rad/s

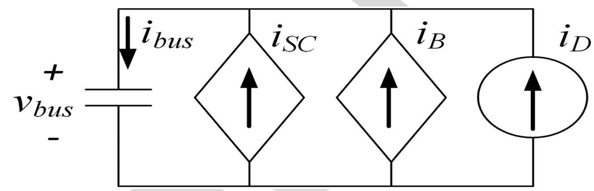

Fig. 4. EMS equivalent circuit for analysis and simulations.

i_{SC}, the battery current i_B, and a disturbance current i_D, which is equal to i_{emsdc} in Fig. 1.

For the equivalent circuit in Fig. 4, the following equations can be written using basic circuit analysis:

$$i_{\text{SC}} + i_B + i_D = sCv_{\text{bus}}. \tag{3}$$

First, let us analyze the HESS controller, when there is no BPF. This is accomplished by removing the BPF block from Fig. 3 and then rewriting (3) by substituting i_{SC}

$$(v_{\text{bus}}^* - v_{\text{bus}}) = \left(K_p + \frac{K_i}{s}\right) - i_B + i_B + i_D. \tag{4}$$

From (4), when the disturbance i_D is zero, the dc voltage transfer function can be derived

$$\frac{v_{\text{bus}}}{v_{\text{bus}}^*}\Big|_{i_D=0} = \frac{sK_p + K_i}{s^2C + sK_p + K_i}. \tag{5}$$

The dc voltage due to the disturbance current, when the reference dc-bus voltage is zero, is

$$\frac{v_{\text{bus}}}{i_D}\Big|_{v_{\text{bus}}^*=0} = \frac{s}{s^2C + sK_p + K_i}. \tag{6}$$

The dc-bus voltage transfer function $v_{\text{bus}}/v_{\text{bus}}^*$ and the dc-bus voltage transfer function with the disturbance current as the input v_{bus}/i_D are plotted in Fig. 5.

The gain for v_{bus}/i_D is greater than 1, which will cause a lot of ripple if there is any ac current present in the disturbance current. The second harmonic current flowing from the dc bus to the ac load is significant and causes dc-bus ripple. This problem can be mitigated by adding a BPF to identify and close a control loop on the second harmonic voltage error.

In contrast to the previous analysis, let us analyze the complete HESS shown in the block diagram of Fig. 3. With the BPF, the dc voltage transfer function becomes

$$\frac{v_{\text{bus}}}{v_{\text{bus}}^*}\Big|_{i_D=0} = \frac{s^3K_p + s^2K_2 + sK_1 + \delta K_i}{s^4C + s^3K_3 + s^2(K_2 + \delta C) + sK_1 + \delta K_i} \tag{7}$$

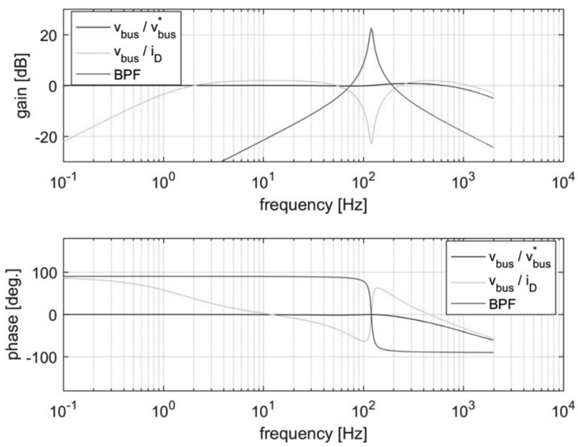

Fig. 5. Bode plots of the transfer functions (5) and (6) without the BPF.

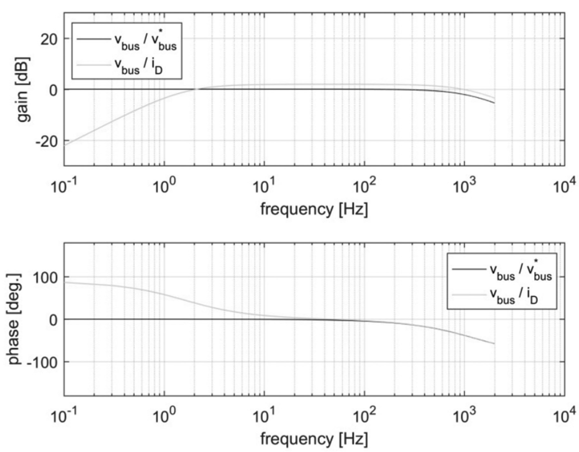

Fig. 6. Bode plots of the transfer functions (7) and (8) with the BPF.

and the dc voltage due to the disturbance current is

$$\frac{v_{\rm bus}}{i_D}\Big|_{v^*_{\rm bus}=0} = \frac{s^3 + \kappa s^2 + \delta s}{s^4 C + s^3 K_3 + s^2(K_2 + \delta C) + sK_1 + \delta K_i}. \tag{8}$$

The coefficients for the transfer functions (7) and (8) are

$$K_1 = \delta K_p + \delta K_i \tag{9}$$

$$K_2 = \kappa K_p + \delta K_i + \beta \tag{10}$$

$$K_3 = \delta K_p + \kappa C. \tag{11}$$

Fig. 6 shows the Bode plots of the transfer functions (7) and (8), where the BPF was added to the control architecture. In contrast with Fig. 5, it can be observed that the addition of the BPF reduces the second harmonic voltage ripple in the dc bus. The BPF has very high gain at 120 Hz, and it reduces the transfer function $v_{\rm bus}/i_D$ significantly at 120 Hz. The BPF has a minimal effect on the transfer function $v_{\rm bus}/v^*_{\rm bus}$.

A time-domain simulation of the system represented in Fig. 1 is shown in Fig. 7. The 120-Hz component of the dc-bus ripple is reduced by the BPF. Also, as shown in Fig. 7, the step response to an increase in the dc load current is reduced. The disturbance current used in the simulation of Fig. 7 is a 10-A sinewave at

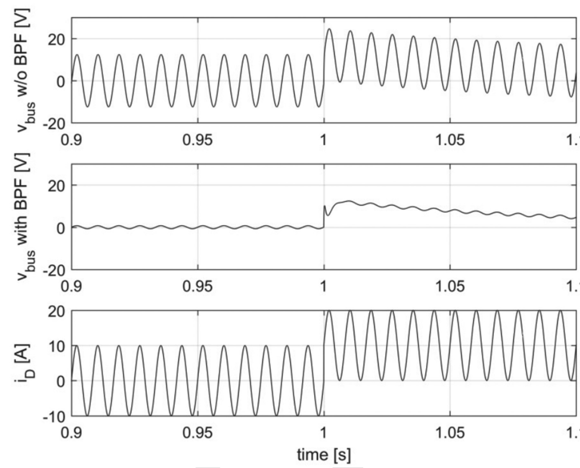

Fig. 7. Time-domain behavior of the HESS controller with and without the BPF for an injected disturbance current i_D ($v_{\rm bus}$ error is shown here).

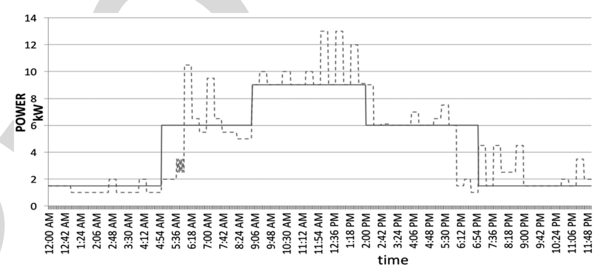

Fig. 8. Load power consumption profile of a remote microgrid, real (DASHED) versus linearized (SOLID) (2-min resolution).

120 Hz plus a 10-A step change in the load current at $t = 1$ s

$$i_D(t) = 10u(t-1) + 10\sin(2\pi 60 t). \tag{12}$$

IV. Lifetime Extension and Economics of an Optimized HESS

In this section, the proposed HESS is used in a remote military microgrid to demonstrate how the above control increases the battery lifetime compared to the same microgrid, where only batteries are used for energy storage. A HESS shows its potential when sudden spikes, not negligible because of the same order of magnitude than the base load, occur. The analysis in this section proves that, when the HESS draws the load transient currents from the SCs, the batteries will last longer. The battery lifetime extension is quantified for different values of the low-pass filter coefficient, and the overall microgrid economics is analyzed.

The power profile of Fig. 8 (dashed line) represents the typical daily consumption in a remote military microgrid, where sudden peaks occur and seriously affect the lifetime of the batteries. This profile is used for the following analysis and case study in contrast to the simplified profile (solid) also plotted in Fig. 8 and used for the study reported in [8].

A. A Few Considerations on the Role of the Optimization

Fuel consumption is one of the parameters that are worth minimizing in a remote military microgrid because fuel

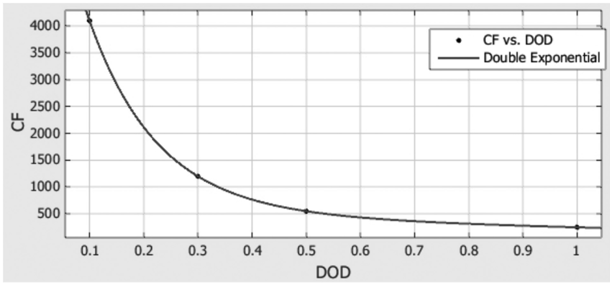

Fig. 9. Reference fitting curve for the lead–acid batteries of the experimental test (CF versus DOD) [26].

transportation to remote sites can result in casualties. In a previous study, the optimization model and its constraints were thoroughly discussed [23]. The results of that optimization are based on 2-min intervals, and it provides the rules for the power sharing among the various sources, taking into account how fast the response from SCs can arrive. These sources include two diesel generators (5 and 15 kW), the PV source (3 kW_P, which is deterministic in the proposed example), and the HESS. In addition, the optimization algorithm ensures that the batteries operate within safe SoC limits, and the generators operate within their range of operation and efficiency. The power associated with HESS, $P_{\rm HESS}$, is thus obtained and is being used in this novel analysis, where the focus is the evaluation of the lifetime of the batteries and the economics of the system, when the controller parameter α varies.

B. Link Between the Controller and the Battery Lifetime

Different battery and SC currents can be obtained by changing the low-pass filter coefficient α, still keeping $P_{\rm HESS}$ constant. With these currents as inputs, we can evaluate the SoC for both devices and find which is the best SoC_* to support the optimized rules

$$\text{SoC}_*(t) = \text{SoC}_*(t-1) - \frac{P_*(t)\Delta t}{\text{ASE}_*}. \tag{13}$$

With SoC_*, P_*, and ASE_*, we identify the SoC, the active power (positive when storage is feeding the load, and negative when is charging), and the storage capacity of each specific device (either the battery or the SCs)

$$P_*(t) = P_{\rm BAT}(t) = v_{\rm bus}(t).i_B(t) \text{ but also}$$

$$P_*(t) = P_{\rm SC}(t) = v_{\rm bus}(t).i_{\rm SC}(t) \tag{14}$$

$$P_{\rm HESS}(t) = P_{\rm BAT}(t) + P_{\rm SC}(t). \tag{15}$$

The currents i_B and $i_{\rm SC}$ must have the same sign, or being 0, meaning that when one device is charging or discharging, the other must act accordingly or it must be OFF.

The battery lifetime is thus assessed by using the Rainflow counting method [24], [25], which needs the results of the SoC over time to provide the number and typology of cycles characterizing the charge and discharge of the battery over a typical horizon. Each kind of battery shows its own cycle to failure (CF) versus depth of discharge (DoD). In Fig. 9, such data for the lead–acid batteries used in the laboratory prototype are reported. We recall that the use of lead–acid batteries is due to safety reasons. Nevertheless, this methodology applies to any kind of battery technology, as long as the CF versus DoD curve can be obtained.

The Rainflow counting algorithm provides information on amplitude (related to the DoD) and frequency of cycles presenting the same amplitude on a set time horizon. The life expectancy of the battery is related to the CF, with 1/CF being the life fraction. We can assess D, the inverse of the lifetime, as

$$D = \sum_{i=1}^{m} \frac{N_i}{\text{CF}_i} \tag{16}$$

where m is the number of different DoD_i, occurring in the set horizon, N_i is the frequency associated with DoD_i, and CF_i is the corresponding number of cycles at DoD_i. For a fully functional battery, D has to be less than 1. When $D = 1$, the battery is considered dead; its unit measure depends on how the number of cycles N_i is counted: if N_i are counted over a day, then the lifetime of the battery (inverse of D) counts the days to failure (DF).

An exemplification: if in a typical day, a battery experiences 10 cycles/day (N), where DoD (the amplitude of the equivalent charge/discharge cycle) is equal to 0.2, then that battery can ideally survive for up to 200 equivalent days, before being considered dead. In fact, $\text{CF@}_{\text{DoD}=0.2}$ is 2000; hence, the lifetime in days $1/D = \text{CF}/N = 200$. When multiple cycles occur, the lifetime is the composition of each single assessment. D depends on N, which relates to DoD; DoD depends on $\text{SoC}_{\rm BAT}$ and SoC depends on the low-pass filter coefficient α; thus, D depends on α.

To sum up the analysis: the higher α, the less current on SC; thus, the lower the lifetime of the battery. To achieve a certain lifetime, we tune the α value, accordingly.

The overall implemented procedure ensures minimum fuel consumption, while suitably tuning the battery lifetime, at the same time. This last objective is achieved by tuning the HESS controller. In the following subsection, we will show how α will also affect the HESS investments and its economics.

C. Case Study Results

In Fig. 10, input and output data, from the optimization procedure described in [23], are reported for the case study: a remote military microgrid. Case A is the reference case when storage is made up only by batteries (no SCs), while case B represents the case when the HESS is present (with SCs). The needed data for both cases, regarding the features of the optimized considered system, deal with the battery, the gensets, and the load profile on a set horizon. In particular, for the battery, the parameters are the following:

1) $\text{SoC}_{\min}$ and $\text{SoC}_{\max}$;
2) charging/discharging efficiency η;
3) rated power $P_{\max}$;
4) discharging/charging time at $P_{\max}$;
5) available capacity.

For gensets 1 and 2, the parameters are the rated powers P_{n1} and P_{n2} and the related relationships between the load factor

	Description	Case B	Case A (Reference)	unit measure	note or symbol
battery	state of charge: range	**0.5-1**	**0.2-1**	p.u	SoC min-max values
battery		SoC(t=0)=SoC(t=end of the day)			typical day assumption
battery	charge/ discharge efficiency	0.9/0.9	0.9/0.9	p.u.	
battery	maximum available constant battery power (rated)	3	3	kW	Pbat max
battery	duration time @ Pbat max	6	6	hours	T
battery	Battery capacity	18	18	kWh	ASE
genset	rated power	5-15	5-15	kW	P1n, P2n
general parameters	a total of 720 t per typical day	2	2	minutes	t step
general parameters	Load in a typical day	Fig.8	Fig. 8	W	PL
results	power from/to the storage	Phess =200*(iB+ iSC)	Pbat= 200*iB	W	
results	power shares among sources	Fig.14	Fig.11		

Fig. 10. Matrix visualization of all the most important input and output information coming from the previous optimization.

and the fuel consumption [8]. Furthermore, the time step t and the load profile P_L shall be established.

Also, Fig. 10 reports in the last row the indication to the resulting output, the balancing of powers to feed the load, meaning the sequence of powers from gensets and to/from the storage unit.

Additionally, for case B, in Table II, technical data of the used basic SC module are reported.

When the DASHED load profile of Fig. 8 is considered for a typical day, the optimized procedure identifies the best $P_{\text{HESS}}(t)$ (or P_{BAT} if no SCs are present) for each time step of the day and for the given conditions.

For case B, we consider three scenarios, cases B1, B2, and B3, identified by different values of the low-pass filter coefficient α, equal to 0.005 (B1), 0.003 (B2), and 0.001 (B3). Once the optimization has produced the power share among the gensets and the storage, then different alphas determine a different sequence for $i_B^{B1,B2,B3}(t)$ and $i_{\text{SC}}^{B1,B2,B3}(t)$ and thus $\text{SoC}_B^{B1,B2,B3}(t)$: superscripts identify the respective scenarios. Similarly, when no SCs are considered, then we will have $i_B^A(t)$ and $\text{SoC}^A(t)$.

TABLE II
SC MAXWELL DATA [27]

Product name	BMOD0130P056 B03
Rated Capacity (F)	130
Rated Voltage (V)	56
ESR (mΩ)	8.1
Leakage current (mA)	120
Absolute maximum current (A)	1,900
max continuous current (A)	61 $\div$ 99
Weight (kg)	18
Stored Energy (Wh)	56.6
$P_{\text{SC}_{\max}}$ (kW)	96.79
t @ $P_{\text{SC}_{\max}}$ (s)	2.11
cost of single unit ($)	1,300

TABLE III
CASE STUDY: MAIN RESULTS FOR THE THREE SCENARIOS (B1, B2, AND B3) AND THE REFERENCE CASE A

Description↓	$\alpha\rightarrow$	**0.005** B1	**0.003** B2	**0.001** B3	**Ref.** case A
SCs capacitance	F	650	910	1300	no SC
set $\text{SoC}_{\min}$		0.5	0.5	0.5	**0.2**
The lowest SoC	%	69.9	67.53	67.06	**30**
Cycles		20	18	16	**51**
Lifetime	days	274	282	363	**122**
Invest. on SC	k$	6.5	9.1	13	N.S.
Invest. on BAT.	k$	10.8	10.8	9.	**25.2**
Tot. Inv. (5y)	k$	17.3	19.9	22.	**25.2**

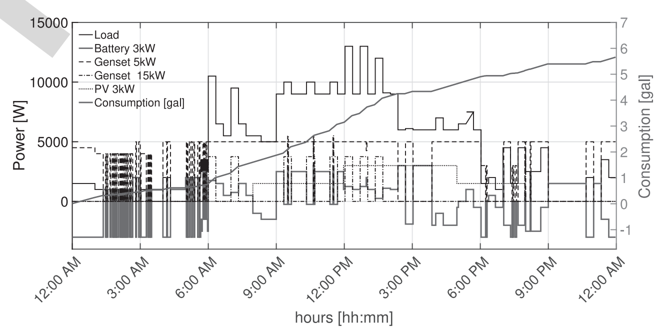

Fig. 11. Case A (only with batteries): from the optimization [23]: power profile and consumption (resolution step 2 min; $\text{SoC}_{\min} = 0.2$).

For each of the four SoC sequences, a new series of $\text{DoD}^{B1,B2,B3,A}$ is derived, and different lifetimes are expected.

In Table III, the main results are reported for the three scenarios [increasing SCs number from 5 (B1) to 10 (B3)], after the optimization and the tuning of α, as well as for the Reference case A, optimized but without SCs.

The investment (INV^i) in each ith scenario/case is thus evaluated as in the following, depending on the DF of the batteries, which ultimately depends on alpha:

$$\text{INV}^i\left(\text{DF}\left(\alpha\right)\right) = \text{INV}_{\text{SC}}^i + \sum_{\text{DF}} \text{INV}_B^i\left(\text{DF}\left(\alpha\right)\right). \qquad (17)$$

The change in i_B and i_{SC} sequences can be visualized when simulating the battery current with and without SCs. In Figs. 11

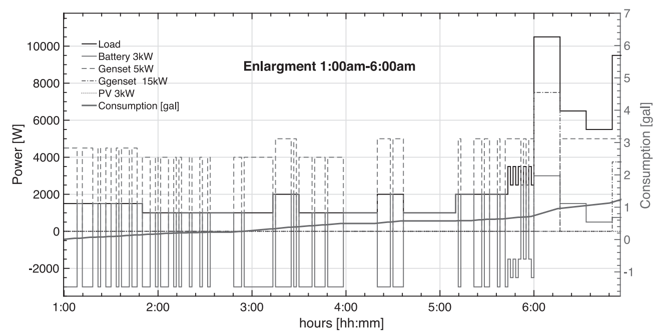

Fig. 12. Case A: Enlargement between 1:00 A.M. and 6:00 A.M. (resolution step 2 min; $\mathrm{SoC}_{\min} = 0.2$).

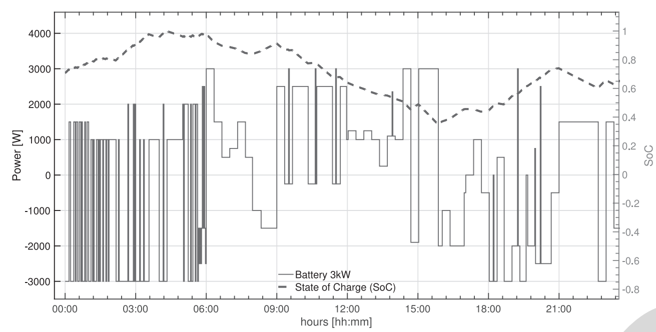

Fig. 13. Case A: Optimal P_{BAT} and consequent SoC on batteries (resolution step 2 min; $\mathrm{SoC}_{\min} = 0.2$).

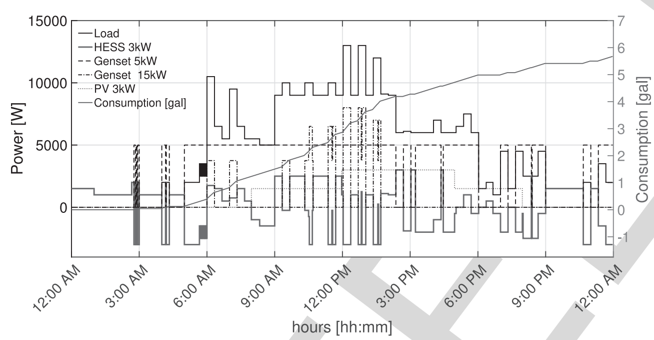

Fig. 14. Case B (with the HESS): from the optimization [23]: power profile and consumption (resolution step 2 min; $\mathrm{SoC}_{\min} = 0.5$) .

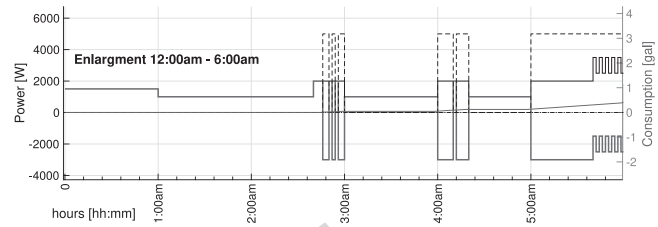

Fig. 15. Case B: Enlargement between 1:00 A.M. and 6:00 A.M. (resolution step 2 min; $\mathrm{SoC}_{\min} = 0.5$).

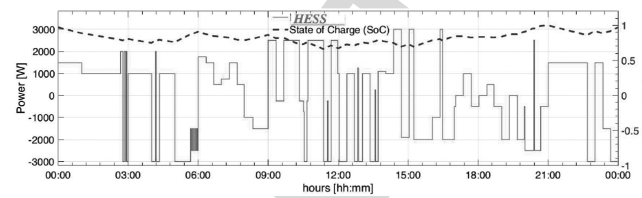

Fig. 16. Case B: Optimal P_{HESS} and consequent SoC on batteries (resolution step 2 min; $\mathrm{SoC}_{\min} = 0.5$).

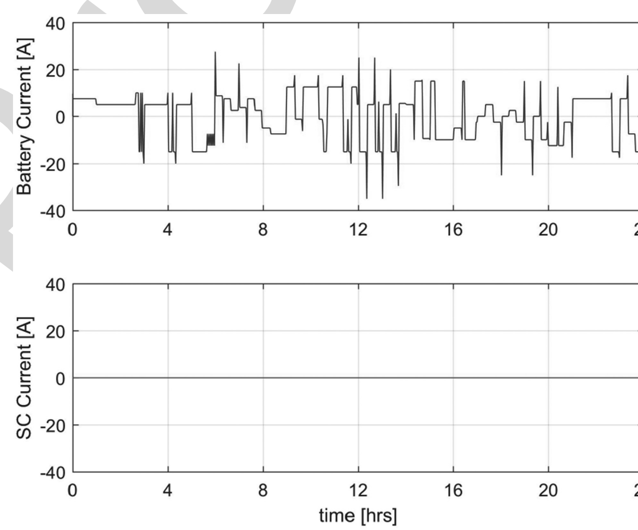

Fig. 17. Case B: battery current when the HESS control system is in place but is disabled (with transient, resolution step 0.1 s). SC current is zero.

and 14, the optimization results are reported for case A (Reference) and for case B: what is referred as HESS profile is the active power associated with what is coming from/to the storage unit (no transient considered, resolution step 2 min).

For a better understanding of the battery dynamic, in terms of charging/discharging cycles and consequent SoC, Figs. 12 and 13 for case A and Figs. 15 and 16 for case B are reported.

They show an enlargement of Figs. 11 and 14, respectively, when SCs are not included (case A) and when they are included (case B).

A Simulink model produced the simulated plots in Figs. 17–19. Omitting the switching behavior of the EMS power converters lead to shorter simulation times for the battery current over a 24-h period (resolution 0.1 s). In Fig 17, the battery current is plotted (upper), when yet the SCs are to be turned ON, the transient is considered, and the resolution step is 0.1 s. In Figs. 18 and 19, battery and SC currents are shown, respectively, when the HESS controller is operational with the low-pass filter coefficient $\alpha = 0.005$ (B1) and $\alpha = 0.001$ (B3). It can be observed that the battery current is much smoother when the HESS controller is used to redirect the peak currents to the SCs, and we can also notice how the α value affects the i_B profile (upper graph of Figs. 17–19).

In Fig. 20 (Scenario B1) and Fig. 21 (Scenario B3), the battery cycles are reported for α equal to 0.005 (smaller SCs) and 0.001 (bigger SCs). The main results are reported in Table III, where the increase in DF (122 estimated days with no SCs, 274 for α = 0.005 up to 363 for $\alpha = 0.001$), the assessment of the lowest SoC, and investments are assessed with respect to the illustrated procedure.

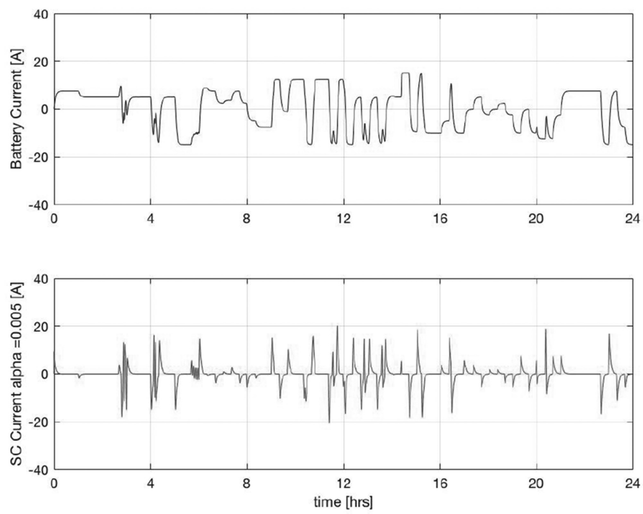

Fig. 18. Scenario B1: battery and SC current when the HESS control system is enable. SCs takes the peaks of the load current (α=.005, resolution step 0.1 s).

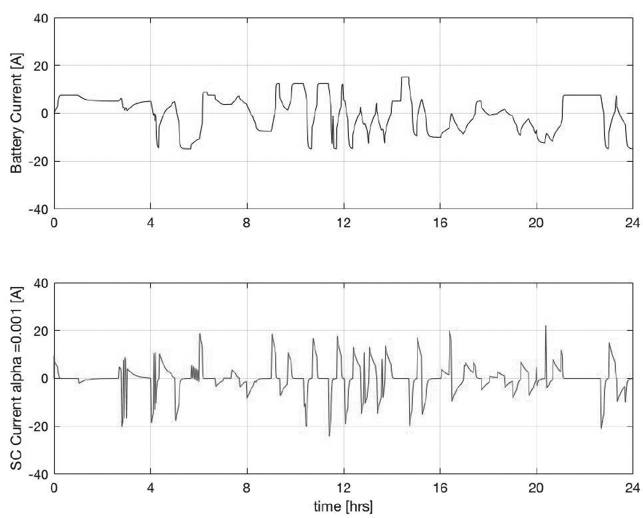

Fig. 19. Scenario B3: battery and SC current with the HESS control system. SCs take the peaks of the load current ($\alpha = 0.001$, resolution step 0.1 s).

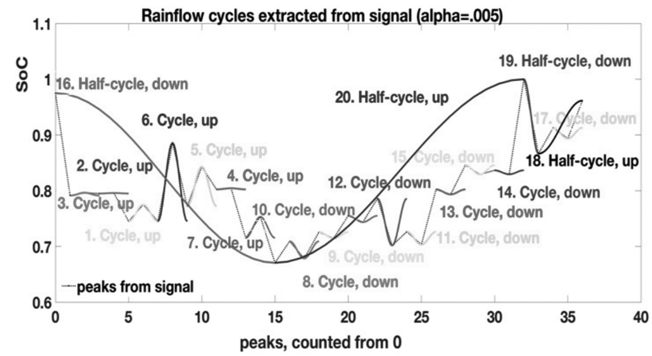

Fig. 20. Scenario B1: Counting cycles at different DoD ($\alpha = 0.005$).

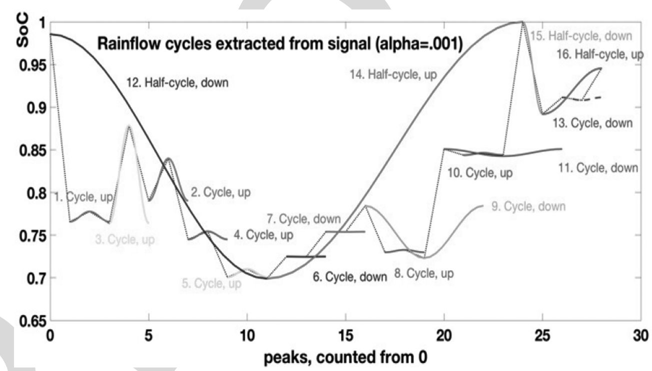

Fig. 21. Scenario B3: Counting cycles at different DoD ($\alpha = 0.001$).

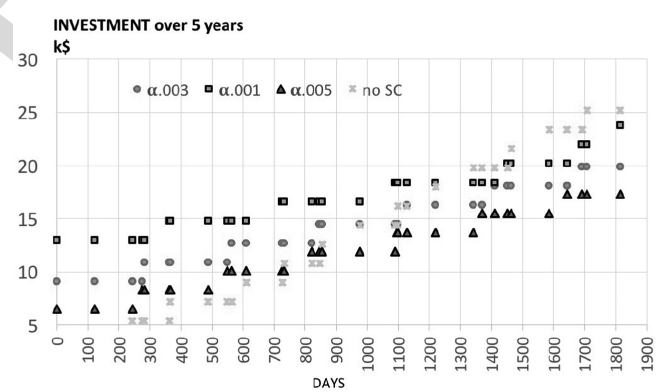

Fig. 22. Investment over five years ($\alpha = 0.005$ blue triangle; $\alpha = 0.003$ orange circle; $\alpha = 0.001$ gray square; yellow star = Reference—NO SCs).

The plots in Fig. 22 and the results in Table III demonstrate how the battery lifetime is extended when the HESS controller is used, realizing the least investment over five years, when α is lower, thus finding the suitable tradeoff between increasing SCs size and the battery wearing out. We can also notice that below ∽900 operating days, even only five SCs modules are not convenient against batteries, but above 900 days, the HESS becomes cost effective. Over ∽1500 days, every investigated HESS is more cost effective than batteries alone.

Depending on the size of the SC and batteries, thus on the deriving cycles to failure, we can infer that the daily power consumption is a key parameter for the economic evaluation. Therefore, careful microgrid load analysis should be done to create a reliable load profile. A sensitivity analysis can also be performed to identify not only the actual optimum, but also the proper range of validity for the current assessment and link it to the controller parameters. This will be illustrated in a future work.

Our methodology makes easily evident how those battery technologies with higher CF versus DoD (for instance, the lithium ones) can positively affect the lifetime assessment because higher CF values directly influence (16). On the other hand, they cost more; thus, again, another sensitivity analysis, focusing on prices, can help in investigating how far our considerations can be stretched.

V. Experimental Measurements

To verify the functionality of the proposed HESS controller, a laboratory experiment was conducted with a scaled-down EMS prototype. The laboratory setup is represented in Fig. 23, where the EMS is included inside the blue box. Note that instead of

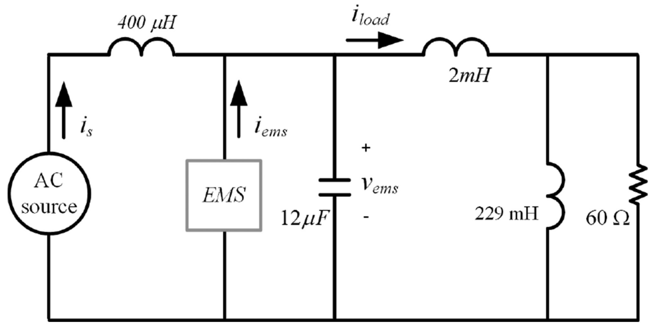

Fig. 23. Schematic of the laboratory setup for the experimental validation.

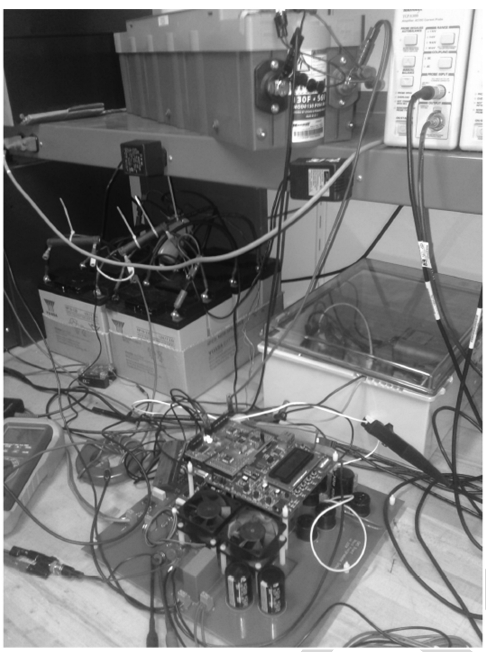

Fig. 24. Photograph of the laboratory setup.

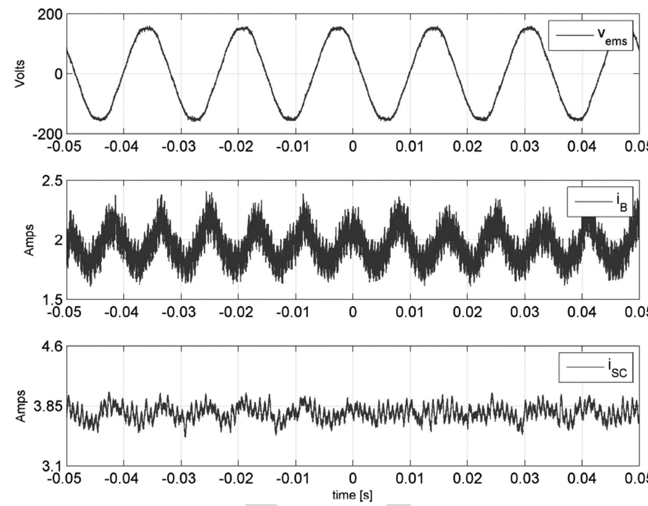

Fig. 25. Case B without HESS controller steady-state experimental waveforms. From the top: ac voltage, battery current, and SC current.

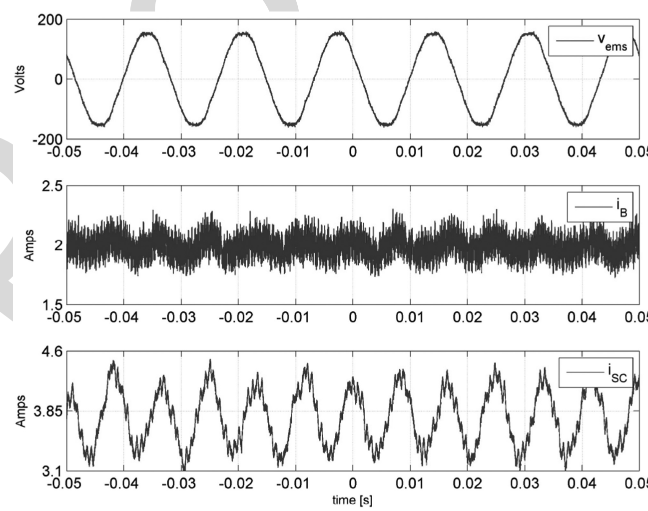

Fig. 26. Case B with HESS controller steady-state experimental waveforms. From the top: ac voltage, battery current, and SC current.

a diesel generator, the ac 120-V 60-Hz power available in the laboratory was used.

A photograph of the prototype on the laboratory bench is shown in Fig. 24. A 130-F Maxwell SC [27] and six Genesis 12-V lead–acid batteries [26] connected in series are visible in the photograph, together with the EMS hardware, which includes several printed circuit boards (PCBs) and external passive components. The EMS controller is embedded on an FPGA, which is part of a Xilinx developed board [28]. The other PCBs are custom made, with the bottom one comprising the power electronics and passive components and the top PCB including A/D converters, USB interface to communicate with a personal computer, and other electronic components that interface with the FPGA board. The code for the FPGA is developed in Simulink with the additional Xilinx System Generator [29] blocks. Further details of the EMS hardware and FPGA software implementation are available in [7] and [9].

The first set of experiments produced the steady-state plots in Figs. 25 and 26 with an without the proposed HESS controller, respectively. The two figures include, from the top, the ac source voltage, the battery current, and the SC current. The contrast between the battery current in Fig. 25 and the battery current in Fig. 26 validates the effectiveness of the HESS controller in removing the 120-Hz frequency component from the battery and sending it to the SC. Harmonic analysis of the battery current from Fig. 25 shows that the amplitude of the 120-Hz harmonic is 158 mA. In contrast, the 120-Hz harmonic of i_B in Fig. 26 is 45.5 mA, a substantial reduction.

A second set of experiments is shown in Figs. 27 and 28, where the dynamic performance of the system is contrasted without and with the HESS controller, respectively. As discussed in previous sections, in order to reduce the charge and discharge cycles on the batteries, the SC is commanded to absorb or deliver currents that are suddenly needed by the microgrid. One example is just before 3:00 P.M. (or 15:00 hours; see Fig. 14); when a large amount of energy is being sent to the HESS and, as shown in Fig. 18, the SC absorbs the initial peak. Fig. 27 demonstrates

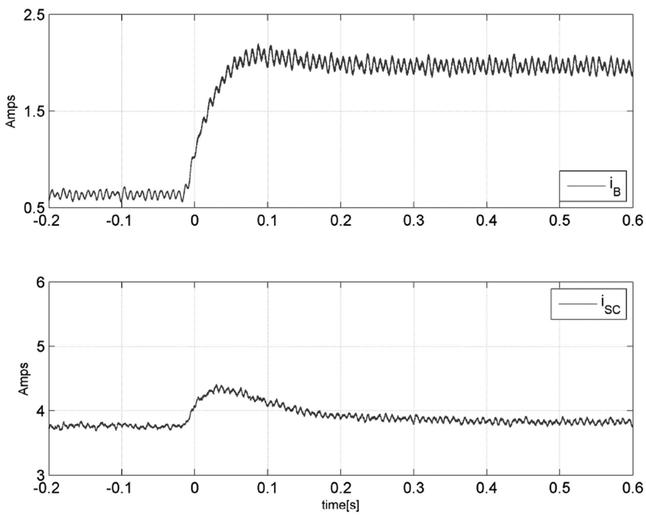

Fig. 27. Battery charge current increase from 1 to 2 A without the HESS controller. Upper i_B and lower i_{SC}.

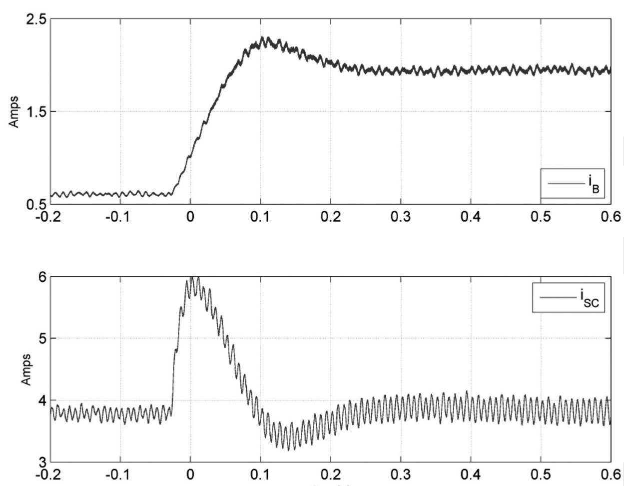

Fig. 28. Battery charge current increase from 1 to 2 A with the HESS controller. Upper i_B and lower i_{SC}.

what happens when the current sent to the battery is doubled from 1 to 2 A: the surge is evident in the battery current, i_B, as well as the 120-Hz ripple. In contrast, the *di/dt* on the battery current i_B is reduced when the HESS controller is turned ON, and also, its ripple is noticeably reduced. Note that $\alpha = 5\,\mathrm{Hz}$ for this experiment.

VI. Conclusion

This paper presents a novel HESS controller focused on increasing the lifetime of the batteries by using SCs with a buck–boost converter to control their charge and discharge, thus maximizing their utilization. A realistic load profile is used, and several scenarios are compared to link the controller parameter α with the battery lifetime extension and to the economic evaluations. Therefore, the economic evaluation is performed on a five-year period, time needed to show when the HESS may become cost effective for the case study. The SCs are sized to take the stress off the load power transients from the battery pack, so that the batteries only "see" an idealized load profile and can perform at better conditions.

Experimental measurements demonstrate the ability of the proposed HESS controller to suppress the 120-Hz ripple from the battery as well as reduce the di/dt when higher currents are commanded. This result proves that the HESS controller redirects higher frequency currents to the SC and leave for the batteries only slow current changes in order to increase the battery lifetime.

Future work will focus on optimizing the number of SCs in order to reduce their economic impact on the microgrid.

Acknowledgment

The authors are grateful to V. Catania for his help with the SC verification and the preceding optimization.

References

[1] G. Quartarone, M. Liserre, F. Fuchs, N. Anglani, and G. Buticchi, "Impact of the modularity on the efficiency of smart transformer solutions," in *Proc. 40th Annu. Conf. IEEE Ind. Electron. Soc.*, 2014, pp. 1512–1518.

[2] J. Rocabert, A. Luna, F. Blaabjerg, and P. Rodríguez, "Control of power converters in ac microgrids," *IEEE Trans. Power Electron.*, vol. 27, no. 11, pp. 4734–4749, Nov. 2012.

[3] A. A. Ferreira, J. A. Pomilio, G. Spiazzi, and L. de Araujo Silva, "Energy management fuzzy logic supervisory for electric vehicle power supplies system," *IEEE Trans. Power Electron.*, vol. 23, no. 1, pp. 107–115, Jan. 2008.

[4] H. Kanchev, D. Lu, F. Colas, V. Lazarov, and B. Francois, "Energy management and operational planning of a microgrid with a PV-based active generator for smart grid applications," *IEEE Trans. Ind. Electron.*, vol. 58, no. 10, pp. 4583–4592, Oct. 2011.

[5] R. Kelly, G. Oriti, and A. Julian, "Reducing fuel consumption at a remote military base: Introducing an energy management system." *IEEE Electrific. Mag.*, vol. 1, no. 2, pp. 30–37, Dec. 2013.

[6] N. R. Tummuru, M. K. Mishra, and S. Srinivas,"Dynamic energy management of renewable grid integrated hybrid energy storage system," *IEEE Trans. Ind. Electron.*, vol. 62, no. 12, pp. 7728–7737, Dec. 2015.

[7] G. Oriti, A. Julian, and N. Peck, "Power-electronics-based energy management system with storage," *IEEE Trans. Power Electron.*, vol. 31, no. 1, pp. 452–460, Jan. 2016.

[8] N. Anglani, G. Oriti, and M. Colombini, "Optimized energy management system to reduce fuel consumption in remote military microgrids," *IEEE Trans. Ind. Appl.*, vol. 53, no. 6, pp. 5777–5785, Nov./Dec. 2017.

[9] G. Oriti, A. Julian, N. Anglani, and G. Hernandez, "Novel hybrid energy storage control for a single phase energy management system in a remote islanded microgrid," in *Proc. IEEE Energy Convers. Congr. Expo.*, Oct. 2017, pp. 1–8.

[10] A. M. van Voorden, L. M. R. Elizondo, G. C. Paap, J. Verboomen, and L. van der Sluis, "The application of super capacitors to relieve battery-storage systems in autonomous renewable energy systems," in *Proc. IEEE Lausanne Power Tech*, Jul. 2007, pp. 479–484.

[11] J. M. Blanes, R. Gutiérrez, A. Garrigós, J. L. Lizán, and J. M. Cuadrado, "Electric vehicle battery life extension using ultracapacitors and an FPGA controlled interleaved buck-boost converter," *IEEE Trans. Power Electron.*, vol. 28, no. 12, pp. 5940–5948, Dec. 2013.

[12] B. Hredzak, V. G. Agelidis, and M. Jang, "A model predictive control system for a hybrid battery-ultracapacitor power source," *IEEE Trans. Power Electron.*, vol. 29, no. 3, pp. 1469–1479, Mar. 2014.

[13] D. B. W. Abeywardana, B. Hredzak, and V. G. Agelidis, "Battery-supercapacitor hybrid energy storage system with reduced low frequency input current ripple," in *Proc. Int. Conf. Renew. Energy Res. Appl.*, Nov. 2015, pp. 328–332.

[14] D. B. W. Abeywardana, B. Hredzak, V. G. Agelidis, and G. D. Demetriades, "Supercapacitor sizing method for energy-controlled filter-based hybrid energy storage systems," *IEEE Trans. Power Electron.*, vol. 32, no. 2, pp. 1626–1637, Feb. 2017.

[15] W. Wei and W. Ping, "A novel power decoupling technique for single-phase photovoltaic grid-connected inverter," in *Proc. 5th Int. Conf. Power Electron. Syst. Appl.*, Dec. 2013, pp. 1–6.

[16] A. M. Gee, F. V. P. Robinson, and R. W. Dunn, "Analysis of battery lifetime extension in a small-scale wind-energy system using supercapacitors," *IEEE Trans. Energy Convers.*, vol. 28, no. 1, pp. 24–33, Mar. 2013.
[17] H. Zhou, T. Bhattacharya, D. Tran, T. Siew, and A. Khambadkone, "Composite energy storage system involving battery and ultracapacitor with dynamic energy management in microgrid applications," *IEEE Trans. Power Electron.*, vol. 26, no. 3, pp. 923–930, Mar. 2011.
[18] S. K. Kollimalla, M. K. Mishra, and N. L. Narasamma, "Design and analysis of novel control strategy for battery and supercapacitor storage system," *IEEE Trans. Sustain. Energy*, vol. 5, no. 4, pp. 1137–1144, Oct. 2014.
[19] W. Jiang, L. Zhang, H. Zhao, H. Huang, and R. Hu, "Research on power sharing strategy of hybrid energy storage system in photovoltaic power station based on multi-objective optimisation," *IET Renew. Power Gener.*, vol. 10, no. 5, pp. 575–583, 2016.
[20] V. I. Herrera, H. Gaztañaga, A. Milo, A. S. de Ibarra, I. Etxeberria-Otadui, and T. Nieva, "Optimal energy management and sizing of a battery-supercapacitor-based light rail vehicle with a multiobjective approach," *IEEE Trans. Ind. Appl.*, vol. 52, no. 4, pp. 3367–3377, Jul./Aug. 2016.
[21] A. Tani, M. B. Camara, and B. Dakyo, "Energy management in the decentralized generation systems based on renewable energy, ultracapacitors and battery to compensate the wind/load power fluctuations," *IEEE Trans. Ind. Appl.*, vol. 51, no. 2, pp. 1817–1827, Mar./Apr. 2015.
[22] J. Aguado, A. J. Sanchez-Racero, and S. de la Torre, "Optimal operation of electric railways with renewable energy and electric storage systems," *IEEE Trans. Smart Grid*, vol. 9, no. 2, pp. 993–1001, Mar. 2018.
[23] N. Anglani, G. Oriti, A. Julian, and V. Catania, "How to control supercapacitors and to account for the consequent extension of battery lifetime in an isolated ac microgrid," in *Proc. IEEE Int. Conf. Environ. Elect. Eng./IEEE Ind. Commercial Power Syst. Eur.*, Jun. 2017, pp. 1–6.
[24] S. Downing and D. Socie, "Simple rainflow counting algorithms," *Int. J. Fatigue*, vol. 4, no. 1, pp. 31–40, Jan. 1982. [Online]. Available: http://www.sciencedirect.com/science/article/pii/0142112382900184
[25] A. Nieslony, MATLAB central-rainflow counting algorithm, 2010. [Online]. Available: http://scholar.google.it/scholar?hl=it&q=adam+nieslony+Rainflow+Counti ng+Algorithm&btnG=&lr=#2
[26] Genesis 150 NP12-12 batteries—specifications. [Online]. Available: http://datasheet.octopart.com/NP12-12-EnerSys-datasheet-10655.pdf. Accessed on: Jun. 5, 2018.
[27] All ultracapacitor Maxwell documents, Nov. 2017. [Online]. Available: http://www.maxwell.com/products/ultracapacitors/downloads
[28] "Xilinx® 'Avnet Virtex-4 LC development board'," Feb. 2018. [Online]. Available: http://www.xilinx.com/products/devkits/DS-KIT-4VLX25LC.htm
[29] *System Generator for DSP—Getting Started Guide*, release 10.1, Xilinx, San Jose, CA, USA, Mar. 2008.

Giovanna Oriti (S'94–M'97–SM'04) received the Laurea (Hons.) and Ph.D. degrees in electrical engineering from the University of Catania, Catania, Italy, in 1993 and 1997, respectively.

She was a Research Intern with the University of Wisconsin, Madison, for two years. After graduation, she joined the United Technology Research Center, where she developed innovative power converter topologies and control. In 2000, she launched her own consulting business developing physics-based models of power converters and drives for electromagnetic interference analysis, stability analysis, and development of control algorithms. In April 2008, she joined the faculty of the Electrical and Computer Engineering (ECE) Department, Naval Postgraduate School (NPS), Monterey, CA, USA, where she is currently a tenured Associate Professor. She holds one U.S. patent and has coauthored 50 papers published in IEEE Transactions or IEEE conference proceedings. Her research interests include power electronic converters for electric ship systems, energy management, microgrids, and renewable energy interface.

Dr. Oriti was the Chair of the Industrial Power Conversion System Department of the IEEE Industry Application Society (IAS) in 2011–2012. She was the recipient of the 2002 IEEE IAS Outstanding Young Member Award. In 2012, she was the recipient of the NPS ECE Service Award in recognition of her contribution to the development of the new NPS EE Energy curriculum. In 2016 and 2017, she was the recipient of the NPS ECE Research Award in recognition of her contributions, through her research, to the U.S. Navy's goal of energy efficiency.

Alexander L. Julian (S'91–M'98–SM'xx) received the B.S.E.E. and M.S.E.E. degrees from the University of Missouri, Columbia, MO, USA, in 1991 and 1992, respectively, and the Ph.D. degree in electrical engineering from the University of Wisconsin–Madison, Madison, WI, USA, in 1998.

After working for two years at the United Technologies Research Center, developing novel power converters for different industrial applications, he contributed to shipboard electronic designs and research for many years as a consultant to Navy vendors by designing, modeling, and prototyping power electronics and motion control systems. From 2004 to 2017, he was a faculty member of the Department of Electrical and Computer Engineering, Naval Postgraduate School, Monterey, CA, USA, being awarded Tenure in 2011. He is currently a consultant. He holds four U.S. patents and has coauthored more than 40 papers in IEEE Transactions or IEEE conference proceedings. His research interests include solid-state power converter design and control, motor drives, electromagnetic interference, reliability and stability analysis for distributed power systems, power converters for renewable energy interface, and microgrids.

Norma Anglani (S'93–M'99) received the Laurea (Hons.) and Ph.D. degrees in electrical engineering from the University of Pavia, Pavia, Italy, in 1993 and 1999, respectively.

After graduating, she worked for a consulting company in the energy efficiency area. Later, she was a Postdoctoral Fellow with the Energy Analysis Group and with the Energy Efficiency Standards Group, Lawrence Berkeley National Laboratory, Berkeley, CA, USA. She is currently an Assistant Professor with the Department of Electrical, Computer and Biomedical Engineering, University of Pavia, Pavia, where she currently teaches and does research in the field of energy management, energy planning, modeling, and efficient compressed air systems. She set up the Labac laboratory, a joint effort between academia and industry. She has been responsible for several research contracts with public and private bodies and has coauthored more than 60 scientific papers.

Dr. Anglani has been a Chartered Engineer since 1995.

Gabriel D. Hernandez received the B.S.E.E. degree from the University of California at Davis, Davis, CA, USA, in 2004, and the M.S.E.E. and E.E. degrees from the Naval Postgraduate School, Monterey, CA, in 2016.

As a U.S. Navy Submarine Officer, he has served aboard the submarine USS OHIO (SSGN 726) and is currently an Engineering Duty Officer managing a submarine-engineered overhaul with Portsmouth Naval Shipyard, Kittery, ME, USA.